Ceramics International 52 (2026) 17248–17267

Contents lists available at ScienceDirect

Ceramics International

journal homepage: www.elsevier.com/locate/ceramint

Thermally driven radiative redistribution in Tb^{3+}-activated $K_2B_4O_7$ borate phosphors for optical thermometry: Effect of alkali co-doping

Abeer S. Altowyan [a,**], M.B. Coban [b,c], U.H. Kaynar [d], S. Cam Kaynar [e], T. Karaman [f], Jabir Hakami [g], H. Aydin [h,i], N. Can [g,*]

[a] Department of Physics, College of Science, Princess Nourah Bint Abdulrahman University, P.O. Box 84428, Riyadh, 11671, Saudi Arabia
[b] Balikesir University, Faculty of Arts and Sciences, Department of Physics, Balikesir, Turkiye
[c] Balikesir University, Science and Technology Application and Research Center, Balikesir, Turkiye
[d] Bakircay University, Faculty of Engineering and Architecture, Department of Fundamental Sciences, Menemen, Izmir, Turkiye
[e] Manisa Celal Bayar University, Faculty of Arts and Sciences, Physics Department, Manisa, 45140, Turkiye
[f] Bakırcay University, Graduate School of Natural and Applied Sciences, Menemen, Izmir, Turkiye
[g] Jazan University, College of Science, Department of Physical Sciences, Physics Division, P.O. Box 114, 45142, Jazan, Kingdom of Saudi Arabia
[h] Central Research Laboratories, Izmir Katip Celebi University, Izmir, Turkiye
[i] Graphene Application &Research Center, Izmir Katip Celebi University, Izmir, Turkiye

ARTICLE INFO

Keywords:
Tb^{3+}-doped borate phosphors
$K_2B_4O_7$
Alkali co-doping
Thermally activated red emission
Radiative redistribution
Optical thermometry
Judd–Ofelt analysis
Temperature-dependent photoluminescence

ABSTRACT

The coupled influence of thermal excitation and alkali co-doping on radiative branching, concentration quenching, and emission redistribution in Tb^{3+}-activated borate phosphors remains insufficiently understood. In this work, $K_2B_4O_7$:Tb^{3+} phosphors were synthesized via solid-state reaction and systematically investigated to establish a quantitative correlation between crystal structure, radiative branching behavior, and ratiometric thermometric performance, with particular emphasis on Li^+/Na^+ co-doping effects. X-ray diffraction and Rietveld refinement confirm a single-phase tetraborate structure, while FTIR and Raman spectra verify preservation of the mixed BO_3–BO_4 framework upon doping. Under 377 nm excitation, the phosphors show intense green emission dominated by the Tb^{3+} $^5D_4 \rightarrow {}^7F_5$ transition, with an optimal activator concentration $x = 0.03$; concentration quenching analysis gives a critical transfer distance $R_c \approx 15.46$ Å, indicating multipolar interaction–driven non-radiative transfer at higher Tb^{3+} contents. Judd–Ofelt analysis quantitatively links local site asymmetry and covalency to radiative transition probabilities, providing a microscopic basis for both concentration quenching and temperature-induced redistribution of branching ratios. Temperature-dependent photoluminescence reveals an unusual anti-correlated response: the dominant green emission undergoes conventional thermal quenching, whereas a red band at ~670 nm increases by ~30-fold between 300 and 550 K, attributed to thermally driven radiative branching redistribution within the $^5D_4$ manifold assisted by phonon-mediated symmetry relaxation. Arrhenius analysis yields an activation energy of ~0.28 eV for undoped $K_2B_4O_7$:Tb^{3+}, which increases with Li^+ co-doping and decreases with Na^+ co-doping, reflecting opposite trends in lattice stiffening and phonon coupling. Time-resolved spectroscopy and radiative rate analysis demonstrate that alkali ions function as active crystal-field and phonon-coupling modulators rather than passive charge compensators, simultaneously tuning defect-assisted non-radiative decay, multipolar interaction dynamics, and intra-manifold branching behavior. Alkali co-doping markedly enhances emission intensity without significant chromaticity drift. Collectively, the combined structural, spectroscopic, thermal, and radiative analyses converge to a unified microscopic mechanism in which alkali-induced lattice perturbations simultaneously modulate multipolar interaction dynamics, radiative branching probabilities, and thermal quenching barriers within the same excited manifold. These findings provide a microscopic framework for alkali-controlled emission engineering and demonstrate that controlled lattice perturbation enables simultaneous tuning of radiative efficiency and thermally driven branching redistribution in a single-ion Tb^{3+} system.

* Corresponding author
** Corresponsing author
E-mail addresses: asaltowyan@pnu.edu.sa (A.S. Altowyan), ncan@jazanu.edu.sa (N. Can).

https://doi.org/10.1016/j.ceramint.2026.02.311
Received 22 January 2026; Received in revised form 17 February 2026; Accepted 19 February 2026
Available online 26 February 2026

1. Introduction

Inorganic borates have received considerable attention as promising host lattices for luminescent materials owing to their excellent chemical and thermal stability, high transparency in the UV–visible region, and structural diversity that enables the incorporation of various rare-earth (RE^{3+}) ions [1–3]. Rare-earth (RE^{3+}) ions are widely recognized for their sharp 4f–4f transitions, long excited-state lifetimes, and emission spanning the visible to near-infrared regions. These properties make RE-doped materials highly attractive for solid-state lighting, display technologies, optical thermometry, and laser applications. For instance, Eu^{3+} and Sm^{3+} are extensively employed in red-emitting phosphors and display systems, while Er^{3+} and Yb^{3+} are widely used in infrared and upconversion-based thermometric platforms. Dy^{3+} and Tb^{3+} ions are particularly valued for their temperature-sensitive green–yellow emissions and high color purity. Recent studies have demonstrated the multifunctional optical potential of RE-doped oxide and glass systems for tunable emission and temperature sensing applications [4–8]. Among these borate hosts, $K_2B_4O_7$ combines a wide band gap (~7 eV), relatively low effective phonon energy, and a non-hygroscopic, structurally stable tetraborate framework, making it an attractive host for efficient rare-earth photoluminescence [9]. The flexible $[B_4O_7]^{2-}$ framework, consisting of corner-shared BO_3 and BO_4 units, provides multiple coordination sites capable of accommodating activator ions with different ionic radii while preserving the structural integrity of the crystal lattice [1]. However, despite these favorable structural and optical characteristics, potassium tetraborate ($K_2B_4O_7$) has so far been investigated predominantly in the context of thermoluminescence applications, particularly when activated with ions such as Cu, Ag, Mn, and Dy [10,11]. Consequently, its photoluminescence behavior—especially under alkali-assisted rare-earth activation—has not yet been systematically explored, making a comprehensive investigation of rare-earth-doped $K_2B_4O_7$ highly warranted. Several other borate hosts with the same $[B_4O_7]$ structural motif, such as CaB_4O_7 [12–14], SrB_4O_7 [15], and MgB_4O_7 [16], have also been explored as luminescent matrices. Despite their favorable properties, these alkaline-earth borates often exhibit relatively limited flexibility for aliovalent substitution without introducing compensating defects, owing to their comparatively rigid lattice frameworks. In contrast, $K_2B_4O_7$ offers superior structural adaptability and ion-exchange capability, allowing fine-tuning of the local environment around RE^{3+} activators. The presence of large K^+ sites facilitates the incorporation of smaller monovalent ions such as Li^+ or Na^+, making it an ideal platform to study co-doping effects and structural-luminescent correlations.

Rare-earth ion doping, particularly with trivalent terbium (Tb^{3+}), has been widely adopted as an efficient strategy for producing intense green emission through the characteristic $^5D_4 \rightarrow {}^7F_J$ (J = 6, 5, 4, 3) transitions. Owing to its well-separated excited states and high color purity, Tb^{3+} serves as an efficient activator for solid-state lighting and optical thermometry applications. However, the luminescence intensity and thermal stability of Tb^{3+}-activated materials are highly sensitive to the host structure and local crystal field environment. In borate matrices, intrinsic lattice distortion and charge imbalance caused by RE^{3+} substitution can lead to the formation of non-radiative centers, thereby quenching the emission efficiency—an issue that can be mitigated through appropriate charge-compensating co-dopants. Very recently, Li^+/Na^+ co-doped Dy^{3+}-activated $K_2B_4O_7$ phosphors have been reported, demonstrating enhanced photoluminescence intensity and improved thermal stability under near-UV excitation [17]. In this context, alkali metal ions such as Li^+ and Na^+ have been shown to play a crucial role in modulating the local structure and optical behavior of RE^{3+}-doped systems. Furthermore, Li^+ and Na^+ co-doping can subtly modify the crystal field around Tb^{3+} ions, influencing the $^5D_4 \rightarrow {}^7F_5$ transition intensity ratio and the overall colorimetric response. Such synergistic effects are particularly advantageous for temperature-sensing applications, where emission intensity ratios or chromaticity shifts are used to evaluate thermal sensitivity. In addition, Li^+ and Na^+ co-doping effectively compensates for charge imbalance induced by Tb^{3+} substitution, supress defect-related non-radiative centers, and improve crystallinity, thereby enhancing energy transfer efficiency and emission stability. Optical thermometry based on Tb^{3+}-activated phosphors typically relies on either the fluorescence intensity ratio (FIR) method or emission color tuning, both of which are strongly dependent on the host's phonon energy and the activator's site symmetry. Borate-based matrices possess moderate phonon energies, which suppress multiphonon relaxation and enable stable luminescence over a wide temperature range. To the best of our knowledge, a direct correlation between alkali-ion-induced structural modification and temperature-dependent photoluminescence behavior in $K_2B_4O_7$:Tb^{3+} has not yet been reported.

Although $K_2B_4O_7$:RE^{3+} phosphors, with or without alkali co-doping, have been mainly investigated in terms of emission enhancement and color tuning, an integrated correlation linking structural characteristics, radiative branching behavior, and ratiometric thermometric performance remains largely unexplored. In particular, the combined structure–PL–FIR thermometry relationship for $K_2B_4O_7$:Tb^{3+} under Li^+/Na^+ co-doping has not been explicitly established.

In this work, $K_2B_4O_7$:Tb^{3+},Li^+/Na^+ phosphors are synthesized via solid-state reaction and systematically investigated to establish structure–property correlations. Structural, vibrational, morphological, and photoluminescence analyses—including temperature-dependent PL and Judd–Ofelt calculations—are employed to evaluate their suitability for optical thermometry and green-emitting phosphor applications. Despite numerous reports on Tb^{3+}-activated borate phosphors, a comprehensive and quantitative structure–radiative–thermometric correlation that directly links alkali-induced lattice perturbations to multipolar interaction dynamics, intra-manifold radiative redistribution, and thermal quenching behavior remains largely unexplored. In particular, the microscopic role of alkali ions in simultaneously regulating defect density, crystal-field symmetry, electron–phonon coupling strength, and radiative branching within a single excited manifold has not been systematically clarified.

In this work, we address this gap by establishing a unified microscopic framework that integrates structural refinement, concentration-dependent energy transfer analysis, Judd–Ofelt radiative parameters, and temperature-driven emission redistribution in $K_2B_4O_7$:Tb^{3+} phosphors. The originality of this study lies in demonstrating thermally driven intra-$^5D_4$ radiative branching redistribution in a single-ion, non-thermally coupled Tb^{3+} system and revealing how alkali co-doping enables controlled modulation of radiative efficiency and thermal quenching barriers through lattice perturbation engineering.

2. Experiments

2.1. Materials and synthesis

$K_2B_4O_7$ host and Tb^{3+}-activated $K_2B_4O_7$:xTb^{3+} ($x = 0.01, 0.02, 0.03, 0.04, 0.05$) phosphors were first synthesized to determine the optimal activator concentration. Based on the concentration-dependent photoluminescence results, the optimal Tb^{3+} concentration ($x = 0.03$) was selected for subsequent alkali co-doping studies. To ensure a controlled evaluation of alkali-induced effects, the Tb^{3+} concentration was fixed at its optimized value, avoiding simultaneous variation of multiple coupled parameters that could complicate the interpretation of co-doping mechanisms. Accordingly, $K_2B_4O_7$:0.03 Tb^{3+} phosphors co-doped with Li^+ or Na^+ at different concentrations (0, 0.5, 1, 2, 3, 5, and 7 wt%) were synthesized via a conventional high-temperature solid-state reaction method. Analytical-grade K_2CO_3 (Sigma-Aldrich, ≥99.0%), H_3BO_3 (Sigma-Aldrich, ≥99.5%), Tb_4O_7 (Sigma-Aldrich, 99.9%), Li_2CO_3 (Sigma-Aldrich, ≥99.0%), and Na_2CO_3 (Sigma-Aldrich, ≥99.0%) were used as starting materials without further purification. These compositions correspond to the samples presented in the XRD patterns (Fig. 1).

The host composition was designed according to the stoichiometry of $K_2B_4O_7$, with appropriate amounts of K_2CO_3 and H_3BO_3 serving as potassium and boron sources, respectively. To compensate for boron volatilization during high-temperature treatment, an additional 5 wt% excess of H_3BO_3 was added to the batch. The Tb^{3+} activator concentration was fixed at 0.03 relative to the host composition, while Li_2CO_3 or Na_2CO_3 was incorporated as a co-dopant in weight percentages of 0–7 wt% with respect to the total precursor mass.

All raw materials were accurately weighed, mixed according to the desired composition, and thoroughly ground in an agate mortar for several hours to achieve a homogeneous precursor mixture. The resulting powders were then placed in alumina crucibles and calcined in a muffle furnace at 750 °C for 5 h under ambient atmosphere using a single-step heat treatment. After calcination, the furnace was allowed to cool naturally to room temperature. The obtained phosphor powders were lightly reground to eliminate agglomeration and stored in a vacuum desiccator prior to structural and optical characterization. For comparison purposes, undoped $K_2B_4O_7$ samples were also synthesized using the same procedure under identical experimental conditions.

2.2. Materials characterization

The phase purity and crystal structure of the synthesized phosphors were analyzed by X-ray diffraction (XRD) using a Malvern PANalytical Empyrean diffractometer operated at 45 kV and 40 mA with Cu Kα radiation ($\lambda = 1.5406$ Å). Fourier transform infrared (FTIR) spectra were collected in the 400–4000 cm^{-1} range using a Thermo Scientific Nicolet iS50 spectrometer in attenuated total reflectance (ATR) mode.

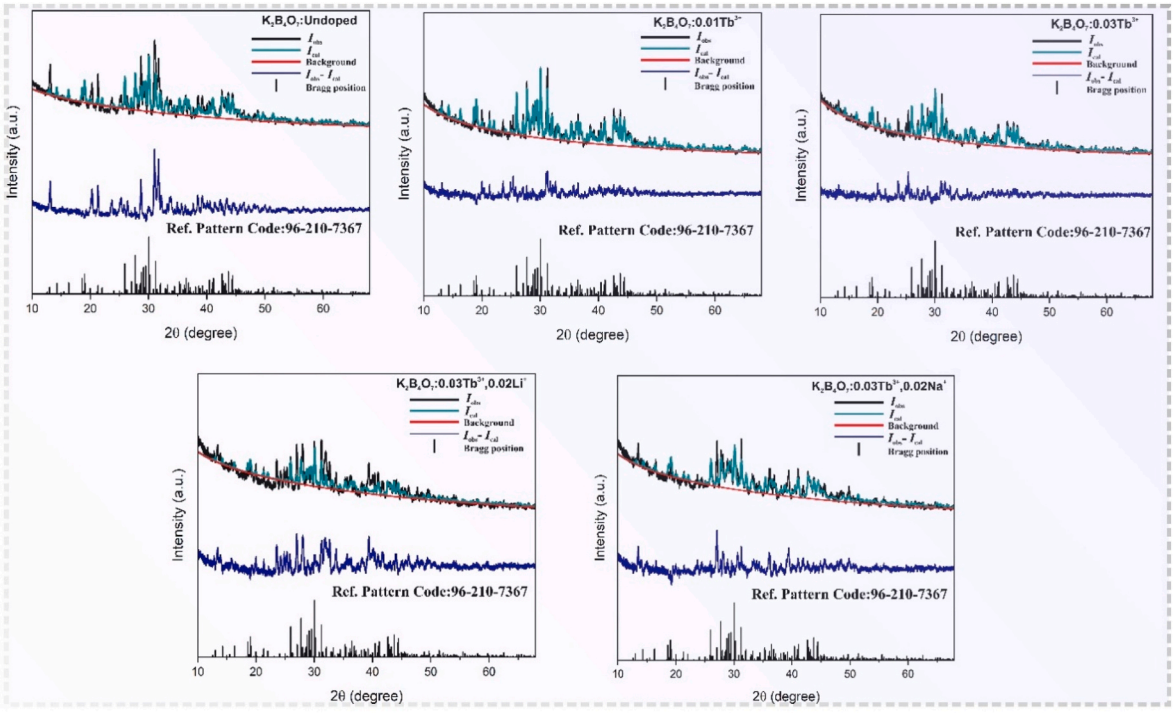

(b)

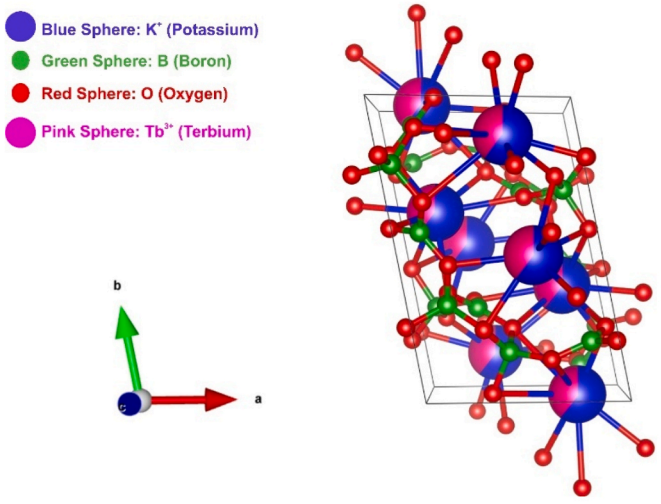

(c)

Fig. 1. (a) X-ray diffraction (XRD) patterns of undoped and doped $K_2B_4O_7$ phosphors. **(b)** Rietveld refinement results of the XRD patterns showing the observed, calculated, and difference profiles. **(c)** Schematic view of the $K_2B_4O_7$ crystal structure illustrating possible Tb^{3+} incorporation and Li^+/Na^+ co-doping sites.

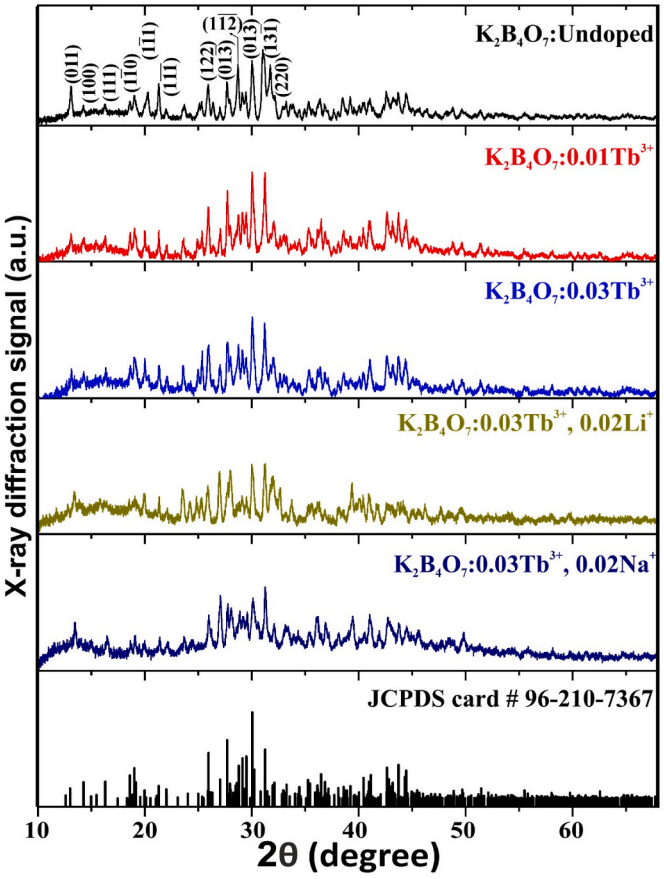

(a)

Fig. 1. (*continued*).

Raman measurements were performed with a Renishaw inVia Raman microscope employing a 532 nm excitation laser to probe the local vibrational modes and bonding characteristics of the host lattice. The surface morphology and elemental composition of the samples were examined using a Zeiss scanning electron microscope (SEM) equipped with an energy-dispersive X-ray spectroscopy (EDS) detector.

Photoluminescence excitation and emission spectra were recorded at room temperature on an Edinburgh Instruments FS5 spectrofluorometer fitted with a xenon lamp and double monochromators. To ensure consistency and reliable comparison, all photoluminescence measurements were conducted under identical experimental conditions for all compositions.

3. Results and discussions

3.1. Structural analysis by X-ray diffraction and rietveld refinement

The crystal structure and phase purity of undoped and doped $K_2B_4O_7$ phosphors were examined by powder X-ray diffraction (XRD). Fig. 1a shows the XRD patterns of undoped $K_2B_4O_7$, Tb^{3+}-doped, and Li^+/Na^+ co-doped $K_2B_4O_7$ samples. All diffraction peaks can be well indexed to the standard tetraborate phase of $K_2B_4O_7$ (PDF No. 98-000-2833), confirming the formation of a single-phase material. No additional reflections corresponding to impurity phases or secondary compounds are observed, indicating that the incorporation of Tb^{3+} and alkali ions does not alter the fundamental crystal structure of the host lattice.

The diffraction profiles remain largely unchanged upon Tb^{3+} doping and subsequent Li^+/Na^+ co-doping, demonstrating the structural stability of the tetraborate framework. Nevertheless, slight variations in diffraction peak intensities and noticeable peak broadening are observed. The relatively broad diffraction peaks can be attributed to the combined effects of lattice microstrain, small coherent crystallite size, and the intrinsically disordered nature of the borate network. Such peak broadening is a well-known characteristic of borate-based materials and does not indicate poor crystallinity or amorphization of the samples.

To further elucidate the structural evolution and quantify the lattice parameter variations induced by doping, Rietveld refinement was performed on all XRD patterns using the reference structure of $K_2B_4O_7$ (PDF No. 98-000-2833). The refinement results, illustrated in Fig. 1b, show good agreement between the observed and calculated diffraction profiles, as evidenced by the low residual difference curves. The reliability factors obtained from the refinements, with R_{wp} values in the range of approximately 0.08–0.13, R_p values of about 0.06–0.12, and χ^2 values between ~2.1 and 4.5, fall within acceptable limits for borate-based systems, confirming the reliability and consistency of the refinement procedure (Table 1).

For the undoped $K_2B_4O_7$ sample, the refined lattice parameters were determined to be $a \approx 6.4976$ Å, $b \approx 9.6162$ Å, and $c \approx 10.4155$ Å, corresponding to a unit cell volume of approximately 622.3 $Å^3$. Upon Tb^{3+} doping and alkali co-doping, only minor variations in lattice parameters and unit cell volume are observed, indicating that the dopant ions induce local structural distortions rather than long-range lattice rearrangements. These subtle changes reflect the influence of ionic size and charge differences while preserving the overall tetraborate framework.

To provide a clearer visualization of the crystallographic environment and possible substitution sites, the crystal structure of $K_2B_4O_7$ is illustrated in Fig. 1c. The structure consists of a three-dimensional $[B_4O_7]^{2-}$ tetraborate framework formed by corner-sharing BO_3 and BO_4 units, with K^+ ions occupying large interstitial sites coordinated by

Table 1
Rietveld refinement results and refined lattice parameters of undoped and doped $K_2B_4O_7$ phosphors.

$K_2B_4O_7$					
Unit Cell	Undoped	0.01 Tb^{3+}	0.03 Tb^{3+}	0.03 Tb^{3+},0.02Li^+	0.03 Tb^{3+},0.02Na^+
a [Å]	6.497	6.492	6.496	6.492	6.492
b [Å]	9.618	9.620	9.624	9.604	9.637
c [Å]	10.415	10.419	10.423	10.418	10.42
α,β,γ [°]	89,77,78	89,77,78	89,77,78	89,77,78	89,77,78
Vol. [Å^3]	622.17	622.229	622.965	621.151	623.309
χ^2	4.501	2.369	2.191	3.475	2.512
R_p	0.121	0.070	0.063	0.096	0.068
R_{wp}	0.165	0.090	0.084	0.125	0.089
R_{exp}	0.036	0.038	0.038	0.036	0.035

oxygen atoms. These spacious K^+ sites offer sufficient structural flexibility to accommodate aliovalent rare-earth ions and alkali co-dopants. The visualization highlights the distinct coordination environments of the cationic sites, supporting the feasibility of Tb^{3+} incorporation accompanied by Li^+/Na^+ co-doping to maintain local charge balance and structural stability.

To rationalize the substitution behavior of Tb^{3+}, Li^+, and Na^+ ions in the $K_2B_4O_7$ lattice, an ionic radius mismatch (D_r) analysis was carried out based on Shannon ionic radii using the relation:

$$D_r = \frac{|R_m(CN) - R_d(CN)|}{R_m(CN)} \times 100\% \quad (1)$$

where R_m and R_d represent the ionic radii of the host cation and dopant ion, respectively, at the same coordination number (CN). In general, a D_r value below 30% is considered favorable for effective substitution in solid-state lattices. The calculated D_r values summarized in Table 2 reveal that direct substitution of Tb^{3+} at the K^+ site exhibits a relatively large ionic radius mismatch, indicating size and charge incompatibility. In contrast, Na^+ ions show a significantly lower D_r value with respect to K^+ sites, suggesting more favorable ionic radius matching and efficient lattice incorporation. Although Li^+ ions exhibit a larger mismatch with K^+ sites, their small ionic radius and high mobility allow them to act as effective charge compensators and lattice modifiers.

Furthermore, the low D_r values calculated between Tb^{3+} and alkali ions support the synergistic role of Li^+/Na^+ co-doping in stabilizing the local coordination environment around Tb^{3+} activators. This cooperative substitution mechanism alleviates lattice strain, suppresses defect formation, and is consistent with the refinement quality obtained from Rietveld analysis. Overall, the combined XRD, Rietveld refinement, and ionic radius mismatch analyses provide strong structural evidence for the successful incorporation of Tb^{3+} and alkali ions into the $K_2B_4O_7$ lattice, establishing a robust structural foundation for the enhanced photoluminescence and optical thermometric performance discussed in subsequent sections.

Although the variations in lattice parameters are small, even subtle local distortions in borate lattices can significantly perturb the crystal-field environment around rare-earth ions. In 4f–4f transitions, the electric-dipole contribution is highly sensitive to local symmetry breaking and changes in ligand polarizability; therefore, minor structural adjustments may strongly influence transition intensities and radiative branching ratios.

In the present $K_2B_4O_7$:Tb^{3+} system, Li^+/Na^+ co-doping modifies the local coordination geometry and strain field surrounding Tb^{3+} activators. Such alkali-induced lattice perturbations are expected to influence the balance between radiative and non-radiative decay channels and may also affect the efficiency of multipolar energy-transfer processes at higher Tb^{3+} concentrations. Consequently, alkali-assisted crystal-field tuning establishes a microscopic structural framework that helps rationalize the observed concentration-dependent emission behavior, alkali-enhanced photoluminescence intensity, and the thermally driven radiative redistribution phenomena discussed in the following sections.

These structural findings indicate that alkali incorporation does not alter the long-range tetraborate framework but introduces controlled local perturbations that are expected to influence crystal-field symmetry and excited-state dynamics of Tb^{3+} ions.

3.2. Proposed substitution and charge compensation mechanism

Based on the combined ionic radius mismatch analysis (Table 2), Rietveld refinement stability, and the absence of impurity phases in XRD patterns, we propose that Tb^{3+} predominantly occupies K^+ sites within the $K_2B_4O_7$ lattice. Although the ionic radius mismatch between Tb^{3+} and K^+ is relatively large, the spacious coordination environment of K^+ sites and the structural flexibility of the tetraborate framework allow aliovalent substitution without structural collapse.

Because Tb^{3+} (3+) substitutes for a monovalent K^+ (1+) site, this aliovalent incorporation introduces local charge imbalance. In the absence of compensation, such an imbalance may promote the formation of intrinsic lattice defects, such as oxygen vacancies (V_o), which can act as non-radiative recombination centers.

Thus, Li^+/Na^+ co-doping provides a more energetically favorable and electrostatically efficient charge-compensation route than defect formation, reducing the likelihood of V_o generation and suppressing defect-assisted non-radiative relaxation pathways. Given the lower ionic radius mismatch of Na^+ relative to K^+, Na^+ is expected to preferentially substitute at K^+ sites, whereas Li^+, owing to its smaller size and higher mobility, may also function as a local lattice modifier or interstitial compensator. Although direct confirmation of site occupancy would require advanced structural probes such as neutron diffraction or EXAFS, the combined structural, compositional, and ionic radius considerations strongly support K-site substitution as the dominant incorporation mechanism in the present system. This substitution model is further supported by the absence of secondary phases and the systematic evolution of radiative properties under alkali co-doping.

3.3. Morphological and compositional analysis

The surface morphology and elemental composition of the undoped and Tb^{3+}-doped $K_2B_4O_7$ phosphors were investigated by scanning electron microscopy (SEM) coupled with energy-dispersive X-ray spectroscopy (EDS). Fig. 2a–c shows the SEM micrographs of the undoped and 0.03 Tb^{3+}-doped $K_2B_4O_7$ samples, respectively. The undoped sample exhibits densely packed, irregularly shaped grains with relatively

Table 2
Ionic radius mismatch (D_r) values calculated using Shannon ionic radii for possible cation substitutions in the $K_2B_4O_7$ lattice.

	K		Tb			K		Li			K		Na	
D_r	R_m	CN	R_m	CN	**D_r**	R_m	CN	R_m	CN	**D_r**	R_m	CN	R_m	CN
31.12	1.51	8	1.04	8	39.07	1.51	8	0.92	8	21.85	1.51	8	1.18	8
	Li		**Tb**			**Na**		**Tb**						
D_r	R_m	CN	R_m	CN	**D_r**	R_m	CN	R_m	CN					
11.53	0.92	8	1.04	8	13.46	1.18	8	1.04	8					

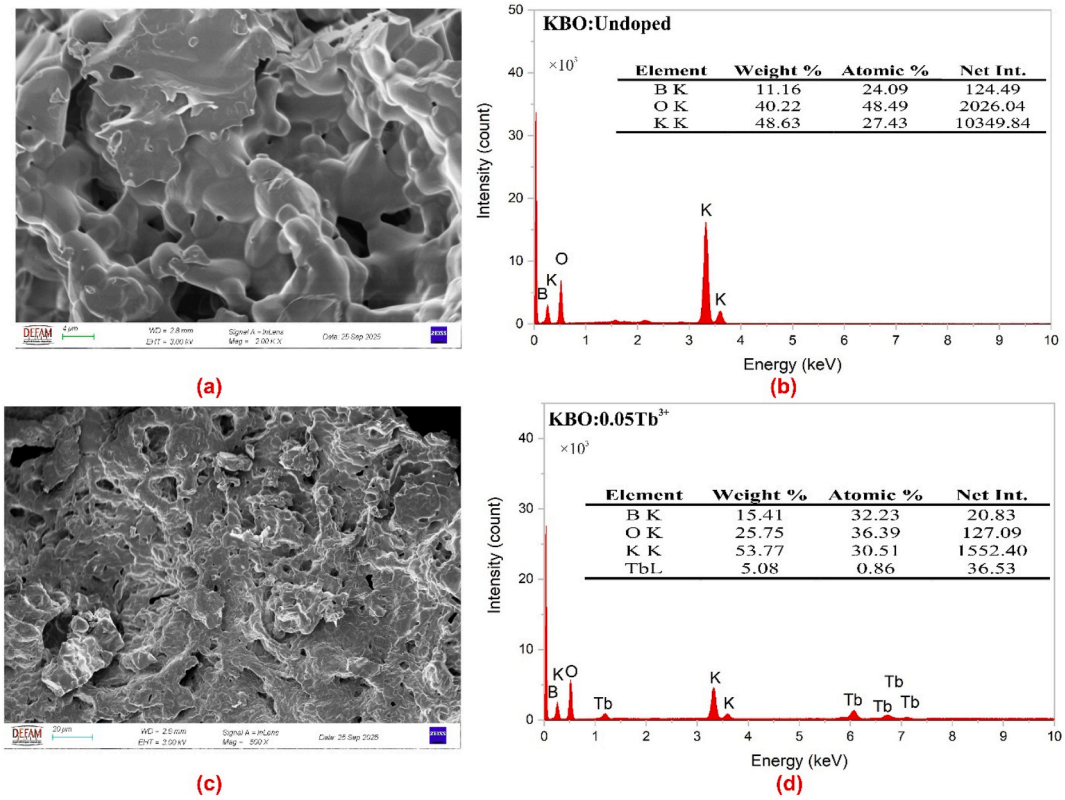

Fig. 2. **(a)** SEM micrograph of undoped $K_2B_4O_7$ showing dense and irregular grain morphology. **(b)** EDS spectrum of undoped $K_2B_4O_7$ phosphor confirming elemental composition. **(c)** SEM micrograph of $K_2B_4O_7$:0.03 Tb^{3+} phosphor revealing morphology modification upon Tb^{3+} doping. **(d)** EDS spectrum of $K_2B_4O_7$:0.03 Tb^{3+} phosphor indicating successful Tb^{3+} incorporation.

smooth surfaces, indicating effective grain growth during the solid-state synthesis process.

Upon Tb^{3+} doping, a noticeable change in surface morphology is observed. The doped sample displays a more porous and interconnected microstructure with elongated and irregular features. Such morphological evolution can be attributed to lattice distortion and modified diffusion kinetics induced by the incorporation of Tb^{3+} ions, which affect grain growth behavior during high-temperature sintering. Similar morphology changes upon rare-earth doping have been widely reported in borate-based phosphors and are often associated with enhanced surface area and defect redistribution.

The elemental compositions of the samples were analyzed by EDS, as shown in Fig. 2(b–d). The EDS spectra confirm the presence of K, B, and O elements in the undoped sample, while the appearance of Tb signals in the doped sample verifies the successful incorporation of Tb^{3+} ions into the $K_2B_4O_7$ host lattice. No extraneous impurity-related elements are detected, indicating the high chemical purity of the synthesized phosphors. The corresponding elemental weight and atomic percentages are summarized in the inset tables, which further support the compositional consistency with the nominal stoichiometry. The uniform distribution of constituent elements and the absence of secondary phases in the EDS analysis are consistent with the XRD and Rietveld refinement results discussed in Section 3.1. The combined SEM–EDS observations thus confirm that Tb^{3+} doping induces controlled morphological modification without compromising phase purity, providing a suitable microstructural foundation for the enhanced photoluminescence and optical thermometric performance of the phosphors.

3.4. FTIR and Raman spectroscopic analysis

The local structural units and vibrational characteristics of undoped and doped $K_2B_4O_7$ phosphors were investigated by Fourier-transform infrared (FTIR) and Raman spectroscopy. These complementary techniques provide detailed insight into the borate network configuration and possible structural modifications induced by Tb^{3+} doping and alkali co-doping.

Fig. 3a presents the FTIR spectra of undoped, Tb^{3+}-doped, and Li^+/Na^+ co-doped $K_2B_4O_7$ samples recorded in the range of 400–4000 cm^{-1}. All samples exhibit a weak and broad absorption band centered around ~3429 cm^{-1}, which is attributed to the stretching vibration of O–H groups arising from adsorbed moisture on the surface of borate materials (Singh& Singh, 2011). The presence of this band is common in borate-based compounds and does not indicate structural hydroxyl incorporation.

The prominent absorption bands observed between ~1400 and 1500 cm^{-1} are assigned to the stretching vibrations of trigonal BO_3 units [18]. Specifically, bands appearing near ~1475 and 1428 cm^{-1} correspond to B–O stretching modes associated with BO_3 structural groups. The bands located in the range of ~1360–1110 cm^{-1} are attributed to asymmetric stretching vibrations of B–O bonds within the borate network [19,20]. Additionally, the absorption features between ~1030 and 770 cm^{-1} are characteristic of B–O stretching vibrations of tetrahedral BO_4 units, confirming the coexistence of BO_3 and BO_4 structural motifs in the $K_2B_4O_7$ lattice. The bands observed below ~750 cm^{-1}, particularly those near ~729, 615, and 569 cm^{-1}, are associated with out-of-plane bending vibrations of B–O–B bridges, while the low-frequency band around ~496 cm^{-1} corresponds to in-plane bending modes of BO_3 units [21].

Importantly, no additional vibrational bands associated with secondary phases or impurity-related species are detected upon Tb^{3+} doping and alkali co-doping. The overall band positions remain nearly unchanged, indicating that the fundamental tetraborate framework is preserved. Minor variations in band intensity and broadening can be attributed to local structural distortion and bond-length redistribution

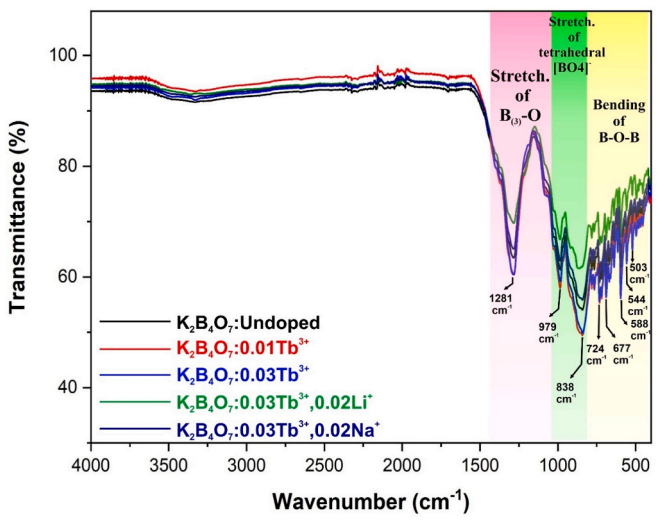

(a)

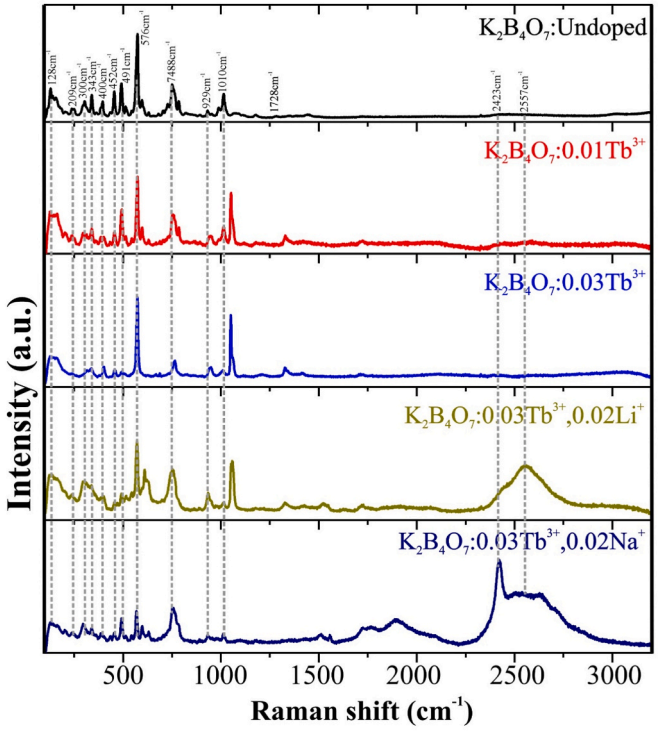

(b)

Fig. 3. (a) FTIR spectra of undoped, Tb^{3+}-doped, and Li^+/Na^+ co-doped $K_2B_4O_7$ phosphors showing characteristic vibrational modes of BO_3 and BO_4 structural units. **(b)** Raman spectra of undoped and doped $K_2B_4O_7$ phosphors illustrating the vibrational features of the tetraborate network and the effect of Tb^{3+} doping and alkali co-doping.

induced by aliovalent substitution and charge compensation effects.

Raman spectroscopy was employed to further probe the short-range structural order and symmetry of the borate network. Fig. 3b shows the Raman spectra of undoped and doped $K_2B_4O_7$ samples recorded in the range of 200–3200 cm^{-1}. The Raman spectra exhibit well-defined bands characteristic of borate-based materials, consistent with the FTIR results. The intense Raman modes observed in the region of ~900–1100 cm^{-1} are primarily associated with symmetric stretching vibrations of BO_4 units, while bands appearing between ~1200 and 1500 cm^{-1} are attributed to stretching vibrations of BO_3 units [19,20]. Low-frequency Raman modes below ~700 cm^{-1} are related to bending vibrations of B–O–B linkages and lattice modes involving K^+ cations.

Upon Tb^{3+} doping and Li^+/Na^+ co-doping, the Raman band positions remain largely unchanged, confirming the structural stability of the tetraborate network. However, slight variations in peak intensity and linewidth are observed, reflecting local symmetry perturbations and lattice strain induced by dopant incorporation. The absence of new Raman-active modes further supports the phase purity of the samples, in agreement with the XRD and Rietveld refinement results discussed in Section 3.1.

Overall, the combined FTIR and Raman analyses confirm that the $K_2B_4O_7$ host lattice retains its characteristic mixed BO_3–BO_4 tetraborate framework upon rare-earth activation and alkali co-doping. The subtle vibrational changes observed are indicative of local structural modification rather than framework disruption, providing spectroscopic evidence for the successful incorporation of Tb^{3+} and charge-compensating alkali ions into the borate network. These results establish a strong structural basis for the observed modifications in PL behavior discussed in subsequent sections.

3.5. Excitation–emission behavior of Tb^{3+}-Doped $K_2B_4O_7$

To examine the intrinsic photoluminescence response of the Tb^{3+}-activated host lattice, a representative Tb^{3+} concentration (3 wt%) was selected. This concentration was not chosen based on optimization considerations; rather, it serves as a practical reference point to capture the general excitation and emission characteristics of Tb^{3+} ions in the host matrix and to establish baseline spectral features for subsequent comparative analysis under different excitation schemes.

As shown in Fig. 4, the excitation spectrum monitored at the dominant green emission ($\lambda em \approx 541$ nm) exhibits several characteristic excitation bands of Tb^{3+} ions in the ultraviolet region, with the most intense band centered at ~377 nm, confirming the effectiveness of near-UV excitation for populating the emitting $^5D_4$ level. Additional excitation features observed below 350 nm correspond to higher-lying 4f excited states (^5K, ^5L, and ^5H manifolds), confirming the well-preserved intra-4f electronic structure of Tb^{3+} in the host lattice and the weak crystal-field perturbation typical of borate-based matrices [22,23].

Under 377 nm excitation, the emission spectrum is dominated by the characteristic $^5D_4 \rightarrow {}^7F_J$ (J = 6–1) transitions of Tb^{3+}, with the strongest emission located at ~541 nm ($^5D_4 \rightarrow {}^7F_5$), producing intense green luminescence. The presence of well-resolved emission lines at 485, 585, 622, 652, and 671 nm further confirms the efficient population of the $^5D_4$ emitting level and negligible competitive emission from the $^5D_3$ state, suggesting effective multiphonon relaxation from $^5D_3$ to $^5D_4$ at this dopant concentration [24,25]. Overall, the excitation–emission behavior demonstrates that the selected Tb^{3+} concentration is sufficient to reveal the fundamental photophysical response of Tb^{3+} in the host lattice without invoking concentration-dependent effects, thereby providing a reliable reference for comparison with spectra obtained under different excitation wavelengths.

Although Tb^{3+}-activated $K_2B_4O_7$ phosphors exhibit excitation-wavelength-dependent emission intensities, presenting emission spectra collected under all possible excitation wavelengths is neither practical nor necessary for a clear physical interpretation. Therefore, representative excitation wavelengths corresponding to the dominant Tb^{3+} 4f–4f absorption bands were selected to evaluate the excitation-dependent emission behavior while maintaining clarity and comparability.

It is noted that excitation at 235 nm produces the highest overall emission intensity among the investigated wavelengths. However, this deep-UV excitation corresponds to high-energy 4f–4f transitions ($^7F_6 \rightarrow {}^5K/{}^5L$ manifolds), which involve excess excitation energy that is rapidly relaxed through multiphonon relaxation before populating the emitting $^5D_4$ level. Similar excitation–relaxation behaviour has been reported for Tb^{3+}-activated borate phosphors under UV and VUV excitation, where higher-lying excited states efficiently relax non-radiatively to the $^5D_4$ level without modifying the emission pathway [26]. As a result,

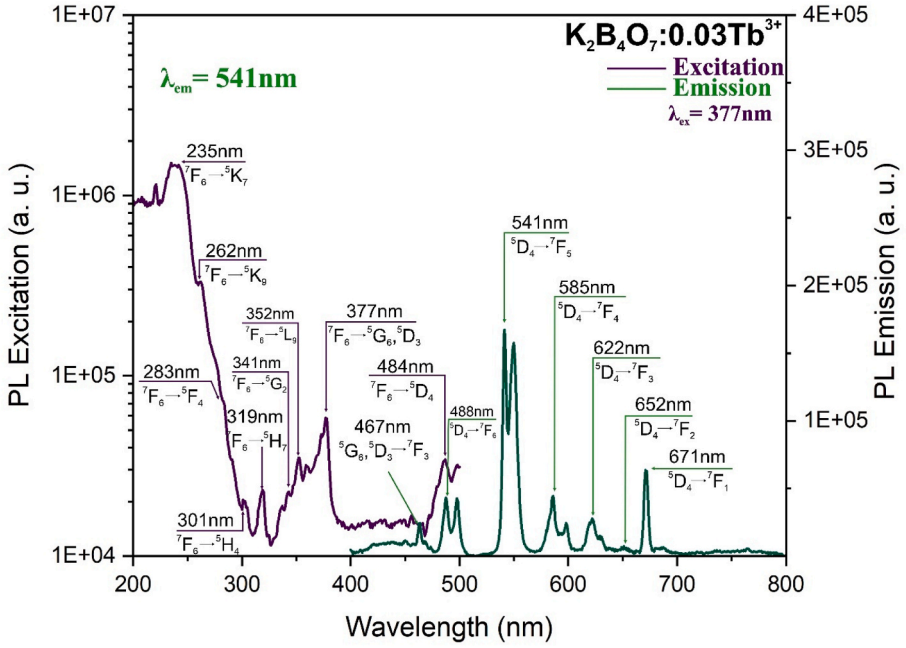

Fig. 4. Photoluminescence excitation spectrum of Tb^{3+}-doped $K_2B_4O_7$ monitored at the green emission ($\lambda_{em} \approx 541$ nm), showing the characteristic *4f–4f* transitions of Tb^{3+} ions in the ultraviolet region. (For interpretation of the references to color in this figure legend, the reader is referred to the Web version of this article.)

although intense emission can be observed, deep-UV excitation is less representative of practical excitation conditions and may overemphasize non-radiative losses as well as host-related absorption contributions. For this reason, excitation wavelengths in the near-UV and blue regions were preferentially considered to probe the intrinsic emission response of Tb^{3+} ions under more physically relevant and application-oriented conditions.

Importantly, regardless of the selected excitation wavelength, the emission spectra consistently exhibit the characteristic $^5D_4 \rightarrow {}^7F_J$ (J = 6–1) transitions of Tb^{3+}, with the green emission ($^5D_4 \rightarrow {}^7F_5$) remaining dominant in all cases. This observation is in good agreement with previous studies on Tb^{3+}-doped borate hosts, where identical emission profiles were observed under UV and even VUV excitation despite large differences in excitation energy [26–28]. This confirms that the excitation wavelength primarily modulates the emission intensity rather than altering the fundamental radiative pathways. The persistence of identical spectral line positions and relative transition patterns indicates that population of the $^5D_4$ emitting level proceeds through efficient non-radiative relaxation channels, leading to an excitation-independent emission profile in terms of spectral shape.

3.6. Emission characteristics, concentration quenching, and alkali Co-doping effects in Tb^{3+}-Doped $K_2B_4O_7$

To systematically investigate the photoluminescence characteristics of Tb^{3+}-activated $K_2B_4O_7$ and the effect of activator concentration on emission efficiency, a series of samples with varying Tb^{3+} contents were examined as shown in Fig. 5a. A representative Tb^{3+} concentration was initially selected to establish the intrinsic emission response of the host lattice without invoking concentration-dependent effects, thereby providing a reliable reference for subsequent comparative analysis.

The excitation spectrum monitored at the dominant green emission ($\lambda_{em} \approx 541$ nm) exhibits a series of sharp bands in the ultraviolet region, characteristic of parity-forbidden 4f–4f transitions of Tb^{3+} ions originating from the $^7F_6$ ground state. The most intense excitation band centered at ~377 nm is attributed to the $^7F_6 \rightarrow {}^5G_6/{}^5D_3$ transition, indicating that near-UV excitation efficiently populates the emitting $^5D_4$ level through non-radiative relaxation. Additional excitation features observed below 350 nm arise from higher-lying 4f excited states (^5K, ^5L, and ^5H manifolds), confirming the well-preserved intra-4f electronic structure of Tb^{3+} in the borate host lattice and the weak crystal-field perturbation typical of borate-based matrices.

Although deep-UV excitation can yield higher emission intensity, near-UV excitation at 377 nm was selected as a more practical excitation condition, minimizing non-radiative losses and host-related absorption effects. For this reason, near-UV excitation at 377 nm was preferentially employed to probe the intrinsic emission behavior of Tb^{3+} ions under more physically relevant and application-oriented conditions.

Under 377 nm excitation, the emission spectra of $K_2B_4O_7$:$x$$Tb^{3+}$ phosphors are dominated by the characteristic $^5D_4 \rightarrow {}^7F_J$ (J = 6–1) transitions of Tb^{3+}, with the green emission ($^5D_4 \rightarrow {}^7F_5$) remaining predominant across all investigated concentrations. As the Tb^{3+} concentration increases from $x = 0.005$ to 0.07, a systematic enhancement in photoluminescence intensity is observed, which can be attributed to the increasing number of optically active Tb^{3+} centers incorporated into the host lattice. The higher activator density enhances the probability of radiative recombination following efficient excitation and energy migration among neighboring Tb^{3+} ions.

When the Tb^{3+} concentration exceeds the optimum value of $x = 0.03$, a pronounced decrease in emission intensity occurs, indicating the onset of concentration quenching. At higher dopant levels, the reduced average distance between Tb^{3+} ions facilitates non-radiative energy transfer processes that compete with radiative emission. To identify the dominant mechanism responsible for concentration quenching, the critical energy transfer distance (R_c) was evaluated based on the experimentally determined optimum concentration and structural parameters obtained from Rietveld refinement. The critical distance represents the average separation between neighboring Tb^{3+} ions at the critical concentration, where radiative and non-radiative energy transfer processes become equally probable. According to Dexter's theory, exchange interactions dominate when $R_c < 5$ Å, whereas multipolar interactions become significant at larger interionic distances. The critical distance R_c was estimated using the following relation:

$$R_c \approx 2\left[\frac{3V}{4\pi x_c N}\right]^{1/3} \quad (1a)$$

where $x_c = 0.03$ corresponds to the experimentally determined optimum Tb^{3+} concentration. The unit-cell volume V was obtained from Rietveld refinement of the XRD data and is found to be 623 Å^3. Considering that Tb^{3+} ions preferentially substitute for K^+ sites in the $K_2B_4O_7$ lattice, the number of available cation sites per unit cell was taken as $N = 8$, corresponding to the total number of K^+ sites (joint available cation sites). Substitution of these parameters into Eq. (1) yields a critical distance R_c of approximately 15.46 Å, which is significantly larger than the critical limit for exchange interactions. This clearly indicates that concentration quenching in the $K_2B_4O_7$:Tb^{3+} phosphor is predominantly governed by multipole–multipole interactions.

To identify the dominant concentration quenching mechanism, the interaction type was analyzed using the Dexter model. Owing to the close energy matching between the $^5D_3 \rightarrow {}^5D_4$ and $^7F_6 \rightarrow {}^7F_0$ transitions, cross-relaxation interactions can occur between neighboring Tb^{3+} ions. However, considering the absence of pronounced $^5D_3$ emission and the relatively large critical transfer distance, exchange and cross-relaxation processes are expected to play only a secondary role in the concentration quenching behavior. Overall, the concentration-dependent photoluminescence results clearly indicate that $x = 0.03$ is the optimal Tb^{3+} concentration for achieving maximum emission efficiency in the $K_2B_4O_7$ host lattice.

To further identify the specific type of multipole–multipole interaction responsible for concentration quenching in the $K_2B_4O_7$:Tb^{3+} phosphor, the relationship between photoluminescence intensity and activator concentration was analyzed using a simplified form of Dexter's theory. Multipolar interactions can generally be classified as dipole–dipole (d–d), dipole–quadrupole (d–q), or quadrupole–quadrupole (q–q), which can be distinguished by evaluating the concentration dependence of the emission intensity.

According to Dexter's model, the interaction mechanism can be determined using the following relation:

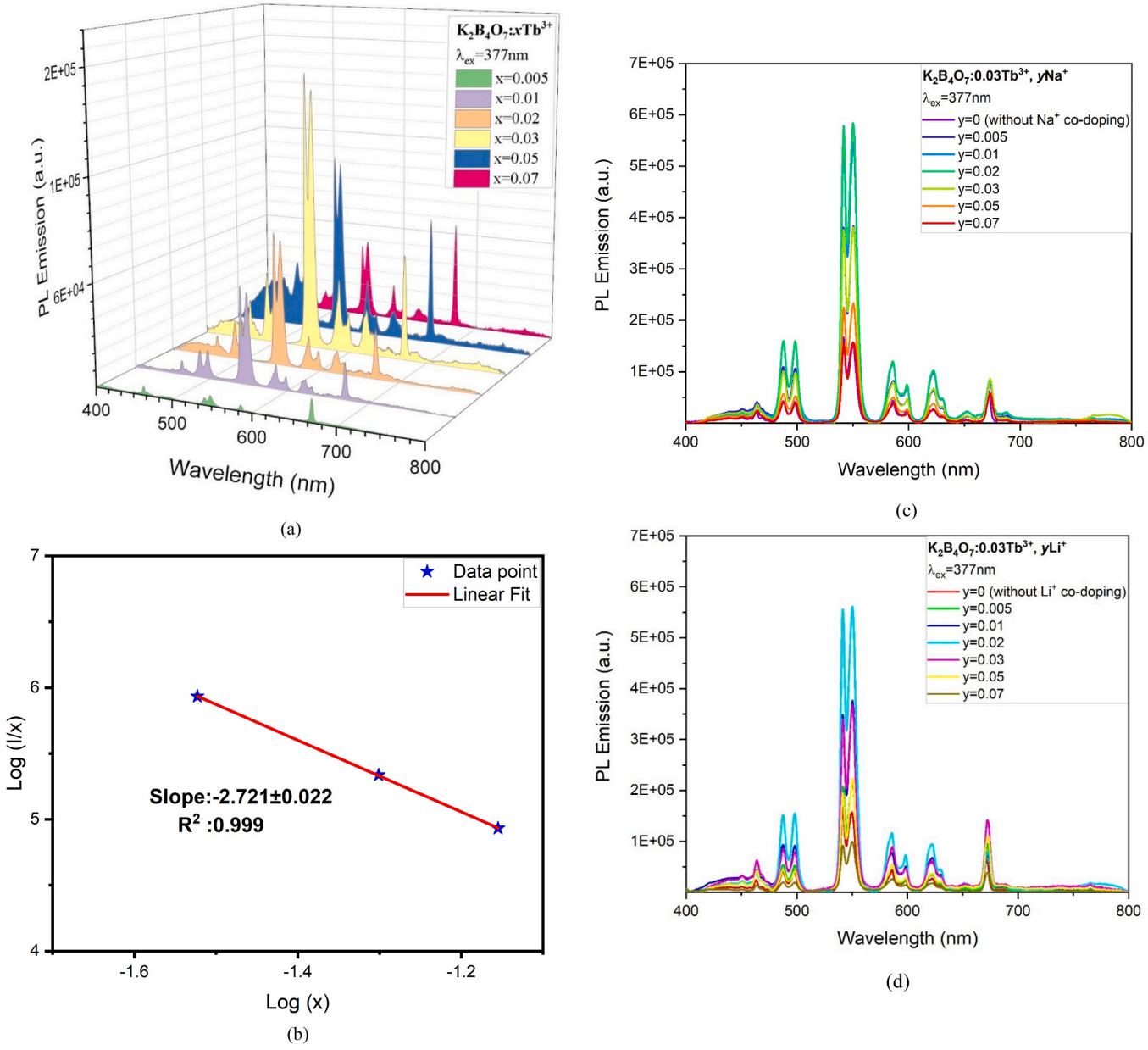

Fig. 5. (a) Concentration-dependent emission intensity of $K_2B_4O_7$:xTb^{3+} phosphors under 377 nm excitation. **(b)** $log(I/x)$ versus $log\ x$ plot with linear fit, indicating dipole–quadrupole interaction (Q ~ 8) as the dominant concentration quenching mechanism. Emission spectra of $K_2B_4O_7$:0.03 Tb^{3+} phosphors co-doped with varying **(c)** Na^+ and **(d)** Li^+ concentrations under 377 nm excitation, illustrating the evolution of Tb^{3+} emission intensity with alkali content.

$$log(I/x) = A - (Q/3)log\,x, \quad (2)$$

where I is the emission intensity, x is the Tb^{3+} concentration, A is a constant, and Q is a characteristic $log(I/x)$ parameter that defines the nature of the multipolar interaction. The values of $Q = 6$, 8, and 10 correspond to dipole–dipole, dipole–quadrupole, and quadrupole–quadrupole interactions, respectively.

Fig. 5b shows the plot of $log(I/x)$ as a function of $log\,x$ for Tb^{3+} concentrations beyond the optimum value, along with a linear fit. The obtained slope of approximately −2.72 yields a Q value close to 8, indicating that dipole–quadrupole interactions dominate the non-radiative energy transfer process responsible for concentration quenching in the $K_2B_4O_7$:Tb^{3+} system. This result is fully consistent with the large critical distance ($R_c \approx 15.46$ Å) obtained from the structural analysis, which excludes exchange interactions and confirms the multipolar nature of the quenching mechanism.

Fig. 5c and d illustrates the effect of alkali co-doping (Li^+ and Na^+) on the photoluminescence behavior of $K_2B_4O_7$:0.03 Tb^{3+} phosphors under 377 nm excitation. In both cases, the characteristic Tb^{3+} emission lines originating from the $^5D_4 \rightarrow {}^7F_J$ transitions remain unchanged in position, indicating that alkali incorporation does not alter the emitting center but primarily influences the local environment and radiative efficiency. As the Li^+ or Na^+ concentration increases, the emission intensity initially rises and reaches a maximum at $y = 0.02$, followed by a gradual decrease at higher alkali contents.

At the optimal composition (0.02Li^+ or 0.02Na^+), the emission intensity is enhanced by approximately 3.7 times compared to the reference $K_2B_4O_7$:0.03 Tb^{3+} sample without alkali co-doping. This pronounced enhancement is attributed to effective charge compensation and defect suppression induced by alkali ions, which reduce non-radiative recombination pathways and improve energy transfer efficiency to the Tb^{3+} emitting centers. Similar alkali-assisted luminescence enhancement has been widely reported in rare-earth-doped oxide and borate phosphors, where monovalent ions such as Li^+ and Na^+ act as efficient charge compensators and lattice modifiers, leading to improved emission efficiency through defect engineering and local structural optimization [29,30]. In addition, the incorporation of small alkali ions locally modifies the crystal field symmetry around Tb^{3+} and reduces high-energy phonon coupling, thereby favoring radiative transitions over multiphonon relaxation. Comparable enhancement mechanisms have also been observed in Dy^{3+}-activated phosphor systems upon $Li^+/Na^+/K^+$ co-doping, further supporting the generality of alkali-assisted defect suppression and crystal-field modulation effects [31]. The subsequent intensity decrease at higher alkali concentrations suggests that excessive co-doping introduces additional lattice distortion and defect states, leading to renewed non-radiative losses.

When compared with the Tb^{3+} concentration-dependent emission behavior shown in Fig. 5a, it is evident that alkali co-doping acts as a secondary optimization parameter. While $x = 0.03$ represents the optimal Tb^{3+} concentration, the introduction of an appropriate amount of Li^+ or Na^+ ($y = 0.02$) further amplifies the emission efficiency without modifying the intrinsic Tb^{3+} emission mechanism. This synergistic effect highlights the crucial role of alkali-assisted defect engineering in maximizing the photoluminescence performance of $K_2B_4O_7$:Tb^{3+} phosphors.

These trends demonstrate a clear correlation between alkali-induced structural perturbations and optical response. Li^+/Na^+ co-doping mitigates the lattice strain associated with Tb^{3+} substitution and partially compensates local charge imbalance, thereby reducing the probability of defect-assisted non-radiative recombination.

Although the dominant concentration quenching mechanism remains governed by dipole–quadrupole interactions, the operation of this multipolar energy-transfer pathway occurs within a locally optimized lattice environment at the optimal alkali content. The reduced defect density and improved local symmetry favor radiative recombination from the $^5D_4$ level, resulting in the observed 3.7-fold emission enhancement.

This microscopic interpretation links alkali-modified local structure to the evolution of concentration quenching behavior and the alkali-optimized luminescence efficiency in $K_2B_4O_7$:Tb^{3+} phosphors.

3.7. Temperature-dependent photoluminescence and thermal quenching behavior of $K_2B_4O_7$:Tb^{3+}

The temperature-dependent photoluminescence behavior of $K_2B_4O_7$:0.03 Tb^{3+} phosphors was investigated to elucidate the thermal stability of the emitting states and to establish a reference framework for subsequent compositional optimization. Fig. 6a presents the three-dimensional emission intensity map as a function of wavelength and temperature under 377 nm excitation. Throughout the investigated temperature range (300–550 K), the spectral positions of the characteristic Tb^{3+} $^5D_4 \rightarrow {}^7F_J$ transitions remain unchanged, indicating that thermal excitation does not induce structural degradation or phase instability of the host lattice. Instead, temperature predominantly affects the emission intensity, reflecting thermally activated excited-state dynamics.

The normalized emission intensity of the dominant green transition ($^5D_4 \rightarrow {}^7F_5$, 541 nm) as a function of temperature is shown in Fig. 6b. With increasing temperature, the emission intensity decreases markedly up to approximately 430–450 K, which can be attributed to enhanced multiphonon-assisted non-radiative depopulation of the $^5D_4$ excited state. At higher temperatures, a partial recovery of emission intensity is observed, suggesting a dynamic competition between thermally activated non-radiative relaxation channels and residual radiative recombination. This behavior indicates that thermal quenching in $K_2B_4O_7$:Tb^{3+} is governed by intrinsic excited-state relaxation processes rather than irreversible thermal degradation.

To quantitatively analyze the thermal quenching mechanism, the temperature dependence of the emission intensity was fitted using an Arrhenius-type model. Fig. 6c displays the linear relationship between ln $[(I_0/I) - 1]$ and 1/kT, where I_0 and I represent the emission intensities at room temperature and elevated temperatures, respectively. The excellent linearity ($R^2 \approx 0.997$) confirms that the quenching process is thermally activated. From the slope of the fitted line, the activation energy for thermal quenching was determined to be $\Delta E \approx 0.28 \pm 0.01$ eV, indicating a relatively high energy barrier separating the radiative $^5D_4$ level from non-radiative relaxation pathways.

The obtained activation energy reflects the favorable phonon environment of the tetraborate framework, which suppresses excessive multiphonon coupling even at elevated temperatures. The persistence of well-defined Tb^{3+} emission features over a broad temperature window highlights the intrinsic thermal robustness of the $K_2B_4O_7$ host lattice. This thermally stable luminescent behavior establishes $K_2B_4O_7$:Tb^{3+} as a reliable platform for high-temperature optical applications and provides a solid baseline for evaluating the influence of compositional modifications—such as alkali co-doping—on thermal quenching dynamics and optical thermometric performance.

The temperature-dependent photoluminescence behavior of the Li^+ co-doped $K_2B_4O_7$:0.03 Tb^{3+},0.02Li^+ phosphor is illustrated in Fig. 7. As shown in Fig. 7a, the spectral positions of the characteristic Tb^{3+} $^5D_4 \rightarrow {}^7F_J$ transitions remain unchanged over the entire temperature range, confirming that Li^+ incorporation does not modify the emitting center or induce thermally driven structural instability. Instead, temperature primarily affects the emission intensity, reflecting intrinsic excited-state relaxation dynamics similar to those observed in the singly doped system.

The corresponding variation of the normalized emission intensity of the dominant green transition ($^5D_4 \rightarrow {}^7F_5$, 541 nm) with temperature is presented in Fig. 7b. With increasing temperature, the emission intensity decreases markedly up to approximately 430–450 K, followed by partial recovery at higher temperatures. This behavior indicates that thermal quenching in the Li^+ co-doped sample remains governed by

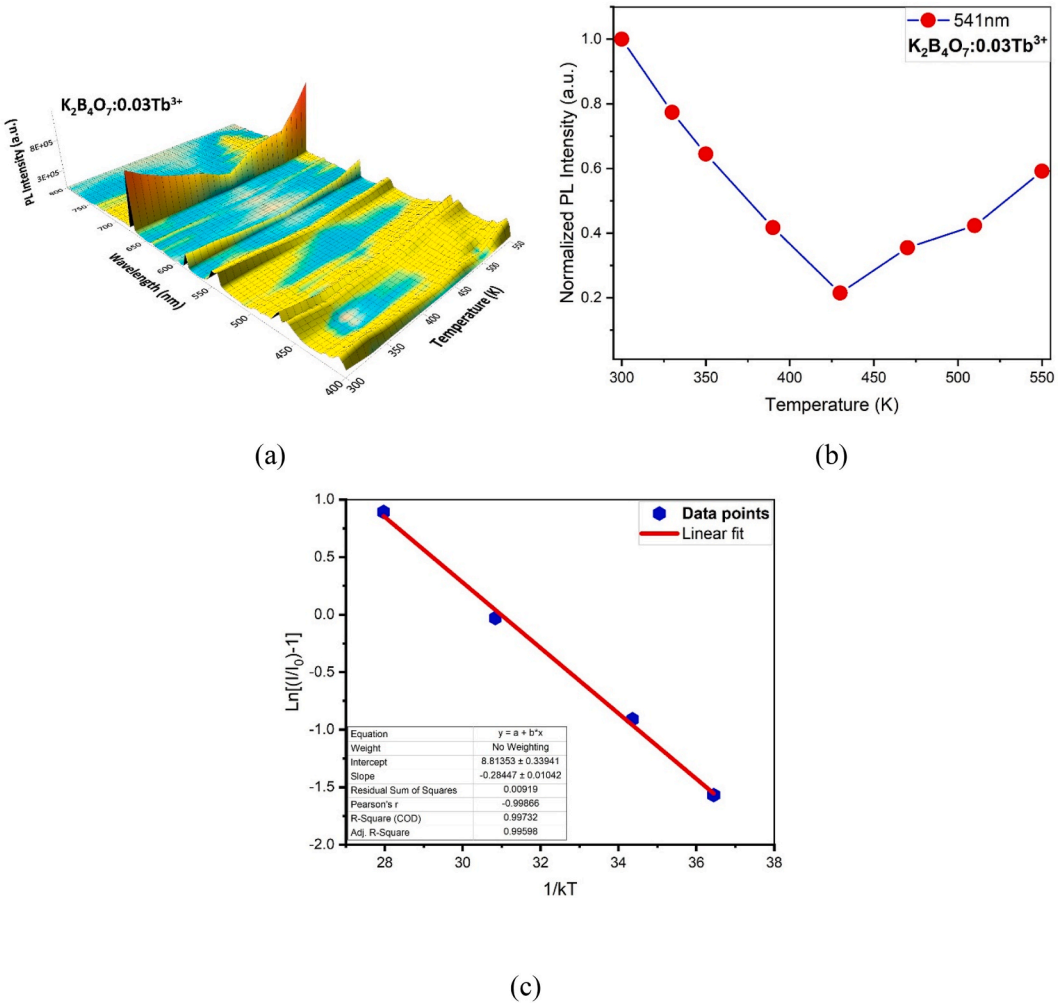

Fig. 6. Temperature-dependent photoluminescence behavior of $K_2B_4O_7$:0.03 Tb^{3+} under 377 nm excitation: **(a)** three-dimensional emission intensity map as a function of wavelength and temperature, **(b)** normalized emission intensity of the dominant green band (541 nm) versus temperature, and **(c)** Arrhenius plot of ln $[(I_0/I) - 1]$ as a function of 1/kT used to extract the activation energy for thermal quenching. (For interpretation of the references to color in this figure legend, the reader is referred to the Web version of this article.)

multiphonon-assisted non-radiative depopulation of the $^5D_4$ excited state, while Li^+ incorporation improves the resistance of the emitting states against thermal deactivation.

Using the same Arrhenius formalism described above, the thermal quenching behavior was further analyzed, as shown in Fig. 7c. An activation energy of $\mathbf{\Delta E \approx 0.34 \pm 0.03\ eV}$ is obtained for the Li^+ co-doped phosphor, which is slightly higher than that of the singly doped $K_2B_4O_7$:0.03 Tb^{3+} sample. The increased activation energy reflects enhanced thermal robustness arising from effective charge compensation and suppression of defect-assisted non-radiative pathways induced by Li^+ co-doping. These results demonstrate that Li^+ incorporation strengthens the thermal stability of Tb^{3+} emission without altering the fundamental quenching mechanism, providing a favorable strategy for improving high-temperature luminescence performance and thermometric reliability.

Fig. 8a presents the three-dimensional temperature-dependent emission map of $K_2B_4O_7$:0.03 Tb^{3+},0.02Na^+ under 377 nm excitation. Similar to the undoped reference, the spectral positions of the Tb^{3+} $^5D_4 \rightarrow {}^7F_J$ transitions remain invariant over the investigated temperature range (300–550 K), confirming that Na^+ co-doping does not induce phase instability or alter the intrinsic electronic structure of the Tb^{3+} emitting centers. Temperature therefore primarily modulates the emission intensity through thermally activated relaxation processes.

The normalized intensity evolution of the dominant green emission ($^5D_4 \rightarrow {}^7F_5$, 541 nm), shown in Fig. 8b, exhibits a thermal quenching trend qualitatively similar to that of the Na^+-free $K_2B_4O_7$:0.03 Tb^{3+} phosphor. However, the onset of quenching occurs at slightly lower temperatures, indicating a modified balance between radiative and non-radiative decay channels upon Na^+ incorporation.

Quantitative analysis using the Arrhenius representation in Fig. 8c reveals a reduced activation energy for thermal quenching compared to the undoped counterpart. From the slope of the linear fit, the activation energy is determined to be $\Delta E \approx 0.17 \pm 0.02$ eV, which is significantly lower than that of $K_2B_4O_7$:0.03 Tb^{3+} without alkali co-doping. This reduction suggests that Na^+ incorporation slightly lowers the energetic barrier separating the radiative $^5D_4$ level from thermally accessible non-radiative relaxation pathways.

Physically, this behavior can be attributed to local lattice softening and modified phonon coupling induced by Na^+ ions. Although Na^+ effectively compensates charge imbalance and suppresses deep non-radiative defects—thereby enhancing room-temperature emission intensity—it also introduces subtle lattice distortions and increases low-energy phonon density around the Tb^{3+} sites. These effects facilitate thermally assisted multiphonon relaxation at elevated temperatures, resulting in a lower apparent activation energy for quenching. Importantly, this reduction does not compromise the overall thermal robustness of the emission but instead reflects a trade-off between enhanced radiative efficiency and slightly increased thermal accessibility of non-

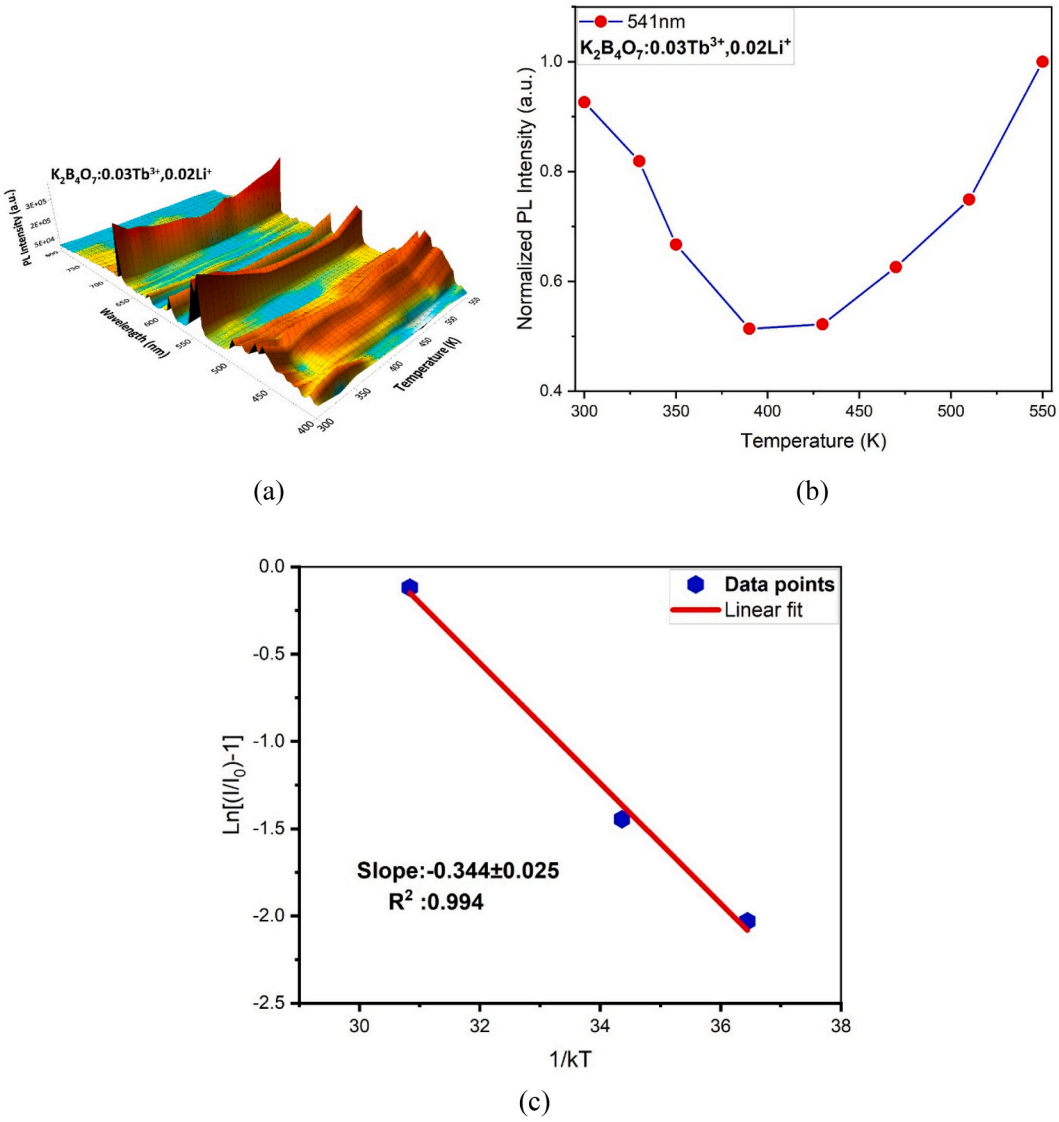

Fig. 7. Temperature-dependent photoluminescence behavior of $K_2B_4O_7$:0.03 Tb^{3+},0.02Li^+ under 377 nm excitation: **(a)** three-dimensional emission intensity map as a function of wavelength and temperature, **(b)** normalized emission intensity of the dominant green band (541 nm) versus temperature, and **(c)** Arrhenius plot of ln $[(I_0/I) - 1]$ as a function of 1/kT used to extract the activation energy for thermal quenching. (For interpretation of the references to color in this figure legend, the reader is referred to the Web version of this article.)

radiative channels.

Overall, the Na^+-co-doped system preserves the favorable temperature-dependent emission characteristics of $K_2B_4O_7$:Tb^{3+} while exhibiting a reduced quenching barrier, an effect that becomes particularly relevant when optimizing the material for temperature-sensitive luminescence and ratiometric optical thermometry.

3.8. Thermally activated red emission and underlying physical mechanism

In addition to the overall thermal quenching of the dominant green emission, a distinctly different temperature response is observed for the emission band centered at ~670 nm, corresponding to the Tb^{3+} $^5D_4 \rightarrow {}^7F_1$ transition. As the temperature increases from 300 to 550 K, this red emission band exhibits a pronounced thermally activated enhancement, with its intensity increasing by approximately 25–30 fold. This behavior stands in sharp contrast to the monotonic quenching of the $^5D_4 \rightarrow {}^7F_5$ green emission and reveals fundamentally different population dynamics governing the two radiative channels.

The observed enhancement of the ~670 nm emission cannot be attributed to a simple increase in the overall excited-state population, as the total photoluminescence intensity decreases with temperature due to thermally activated non-radiative relaxation. Instead, this anomalous behavior indicates a temperature-induced redistribution of radiative branching probabilities within the $^5D_4$ manifold. The $^5D_4 \rightarrow {}^7F_1$ transition is known to be weak and partially hypersensitive to local symmetry and crystal-field perturbations. At elevated temperatures, enhanced lattice vibrations and phonon-assisted distortions locally relax the site symmetry around Tb^{3+} ions, thereby increasing the electric-dipole contribution to this otherwise weak transition and significantly amplifying its radiative probability.

In parallel, thermally activated release of carriers or excitation energy from defect- or trap-related states inherent to the borate host lattice may contribute to preferential feeding of the lower-energy red-emitting channel. Such trap-assisted energy transfer processes become increasingly efficient at elevated temperatures, selectively populating specific $^5D_4$ sublevels that favor red emission. The persistence of narrow line widths and invariant peak positions with increasing temperature confirms that the ~670 nm band originates from intrinsic Tb^{3+} 4f–4f transitions rather than from broad defect-related emission, reinforcing

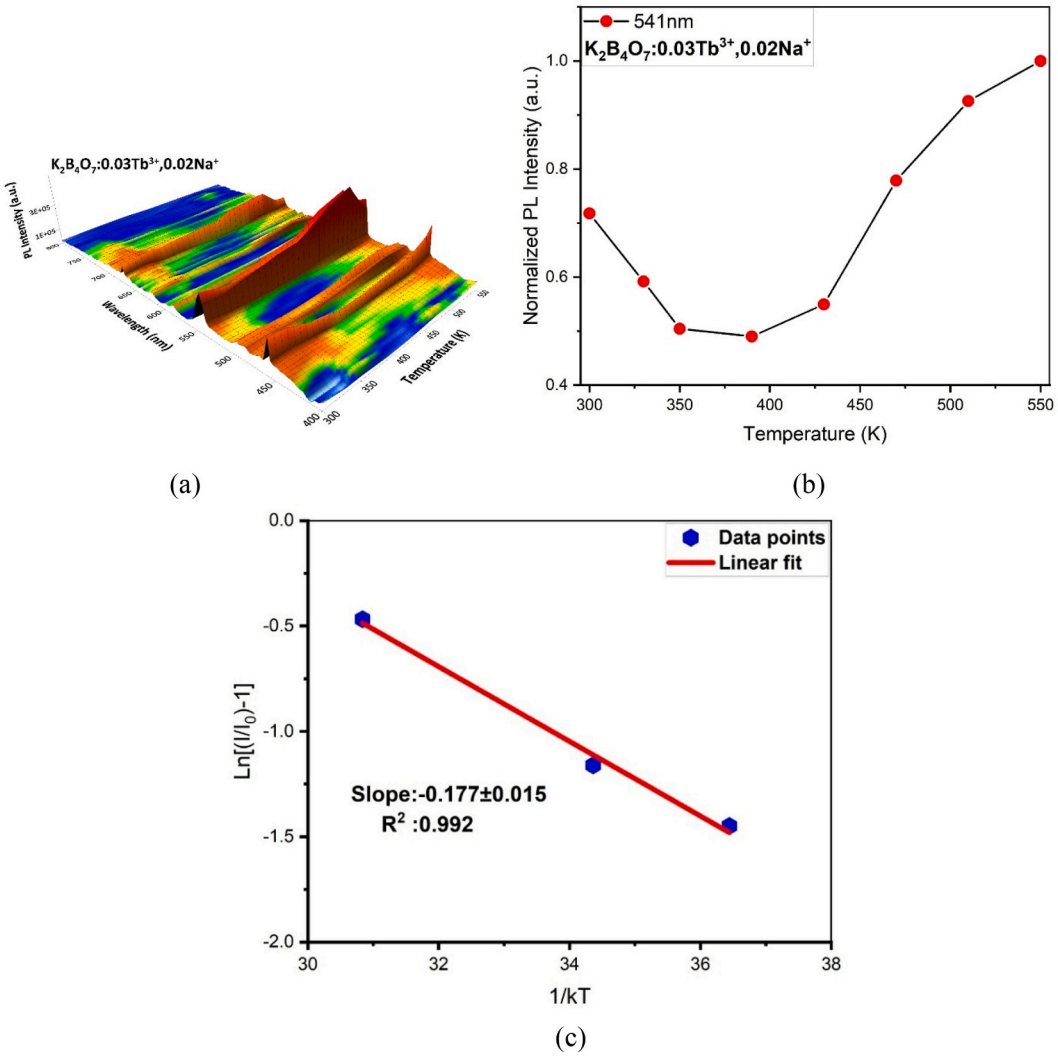

Fig. 8. Temperature-dependent photoluminescence behavior of $K_2B_4O_7$:0.03 Tb^{3+},0.02Na^+ under 377 nm excitation: **(a)** three-dimensional emission intensity map as a function of wavelength and temperature, **(b)** normalized emission intensity of the dominant green band (541 nm) versus temperature, and **(c)** Arrhenius plot of $\ln[(I_0/I) - 1]$ as a function of 1/kT used to extract the activation energy for thermal quenching. (For interpretation of the references to color in this figure legend, the reader is referred to the Web version of this article.)

the interpretation of a genuine thermally assisted radiative redistribution mechanism.

To quantitatively capture this anti-correlated thermal behavior, the fluorescence intensity ratio (FIR), defined as I_{671}/I_{541}, was evaluated as a function of temperature (Fig. 9). As shown, the FIR increases monotonically from ~5.6 at 300 K to ~10.3 at 550 K, reflecting the simultaneous thermal activation of the red-emitting channel and quenching of the green emission. This strong and continuous increase demonstrates that temperature induces a progressive redistribution of radiative decay pathways within the same $^5D_4$ excited state, rather than activating an independent emission center.

The smooth, non-saturating FIR–temperature dependence further indicates that the underlying mechanism is governed by phonon-assisted symmetry relaxation and thermally enabled energy redistribution, rather than abrupt defect ionization or phase-related effects. Such a monotonic FIR response over a broad temperature window is highly desirable for ratiometric optical thermometry, as it provides enhanced sensitivity and intrinsic self-referencing capability based on emissions from a single activator ion.

While the absolute intensity of the ~671 nm red emission increases by approximately 25–30 fold over the investigated temperature range, the corresponding fluorescence intensity ratio (FIR = I_{671}/I_{541}) increases by about 85%, reflecting the combined effect of thermally activated red emission and concurrent quenching of the green emission. Such a wide dynamic range further confirms the robustness of the thermally activated red-emission channel relative to the quenched green emission. The relative sensitivity (S_r), defined as $S_r = \frac{1}{FIR}\frac{d(FIR)}{dT}$, reaches a maximum value of approximately 4.2×10^{-3} K^{-1} in the intermediate temperature region (~450–470 K), where the competition between radiative branching redistribution and multiphonon-assisted non-radiative decay is most pronounced.

This sensitivity is comparable to or higher than many reported Tb^{3+}-based single-ion ratiometric thermometers, highlighting the intrinsic advantage of exploiting thermally activated intra-$^5D_4$ radiative branching rather than thermally coupled excited states. According to recent reviews on FIR-based optical thermometry, most reported systems rely on thermally coupled excited states, whereas non-thermally coupled strategies have been identified as an effective alternative for extending the operating temperature range and improving signal discriminability [32]. In this context, the present $K_2B_4O_7$:Tb^{3+} system represents a non-thermally coupled single-ion FIR thermometer with a broad monotonic response and without saturation. For comparison, Tb^{3+}/Eu^{3+} co-doped phosphors employing energy-transfer-assisted FIR mechanisms typically exhibit relative sensitivities in the 10^{-3}–10^{-2} K^{-1}

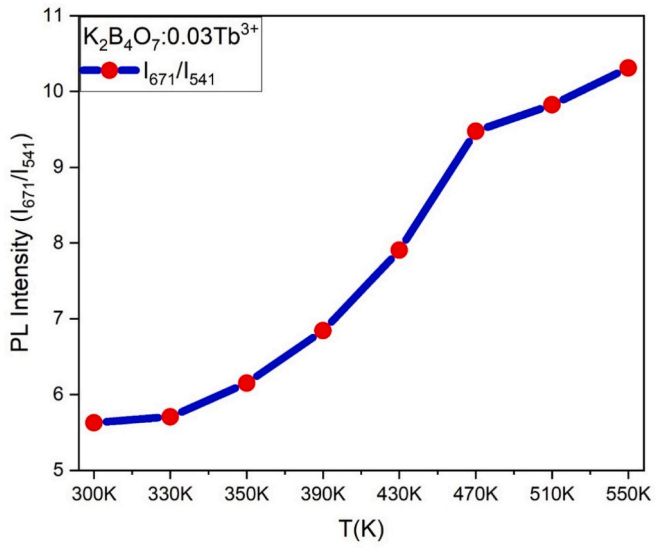

Fig. 9. Temperature dependence of the fluorescence intensity ratio (FIR = I_{671}/I_{541}) for $K_2B_4O_7$:0.03 Tb^{3+} phosphors under 377 nm excitation, showing a monotonic increase from 300 to 550 K due to thermally activated red emission and simultaneous quenching of the green emission. (For interpretation of the references to color in this figure legend, the reader is referred to the Web version of this article.)

range. For instance, Lig et al. reported a maximum Sr of 0.76 % K^{-1} for $Sr_3TaGa_3Si_2O_{14}$:Tb^{3+},Eu^{3+} based on the FIR of Tb^{3+} and Eu^{3+} emissions [33]. In contrast, the present $K_2B_4O_7$:Tb^{3+} phosphor achieves a comparable sensitivity level using a single-ion, non-thermally coupled FIR strategy based on intra-$^5D_4$ radiative branching, offering a simpler and intrinsically self-referenced temperature-sensing platform.

Importantly, because both emission bands originate from the same Tb^{3+} activator, the FIR-based temperature sensing is inherently self-referenced, minimizing uncertainties arising from excitation power fluctuations, concentration inhomogeneity, or optical alignment. These features establish $K_2B_4O_7$:Tb^{3+} as a highly reliable platform for high-temperature ratiometric optical thermometry.

Notably, a similar thermally activated red-emission behavior is also observed in Li^+- and Na^+-co-doped $K_2B_4O_7$:0.03 Tb^{3+} phosphors. While alkali co-doping substantially enhances the overall emission intensity, the temperature dependence and relative enhancement pattern of the ~670 nm emission closely follow that of the singly doped $K_2B_4O_7$:0.03 Tb^{3+} sample. This indicates that alkali incorporation does not introduce a new thermal activation pathway but rather amplifies the existing radiative redistribution mechanism by improving charge compensation and suppressing non-radiative defect centers.

The simultaneous quenching of the green emission and enhancement of the red emission results in a strongly temperature-dependent intensity ratio between the two bands. This anti-correlated thermal response reflects a competition between multiphonon-assisted non-radiative depopulation of the $^5D_4$ level and temperature-driven modification of radiative branching pathways. Such behavior is particularly advantageous for optical thermometry, as it enables ratiometric temperature sensing based on emissions originating from the same activator ion, thereby minimizing errors associated with excitation fluctuations or concentration inhomogeneities.

Overall, the pronounced thermally activated enhancement of the ~670 nm emission, together with the strongly temperature-dependent FIR, highlights the complex interplay between lattice dynamics, local crystal-field symmetry, and excited-state relaxation pathways in $K_2B_4O_7$:Tb^{3+}. These results establish a solid physical basis for exploiting the FIR (I_{671}/I_{541}) as a robust thermometric parameter, positioning this system as a promising candidate for high-sensitivity ratiometric optical thermometry and high-temperature luminescent sensing applications.

From a microscopic standpoint, alkali incorporation modulates both the local symmetry and the electron–phonon coupling strength around Tb^{3+} activators. Such modifications directly influence the activation energy for thermal quenching as well as the relative radiative branching probabilities within the $^5D_4$ manifold.

Li^+, owing to its smaller ionic radius and stronger local field effect, tends to stiffen the local lattice environment and increase the energetic barrier for multiphonon relaxation, resulting in a higher quenching activation energy. In contrast, Na^+ induces slight lattice softening, which lowers ΔE and enhances thermal accessibility of non-radiative channels.

Consequently, alkali co-doping tunes the dynamic competition between multiphonon-assisted depopulation of the $^5D_4$ level and thermally driven radiative redistribution among its sublevels. This unified microscopic picture consistently links alkali-induced structural perturbations to modified phonon coupling strength and to the experimentally observed anti-correlated green–red thermal response.

3.9. Radiative lifetime dynamics and quantum efficiency analysis

To further understand the impact of alkali co-doping on the energy relaxation pathways of Tb^{3+} ions in the $K_2B_4O_7$ host, time-resolved photoluminescence decay measurements were conducted for the $^5D_4 \rightarrow {}^7F_5$ transition. The luminescence decay curves (Fig. 10) exhibited a biexponential character for all compositions, consistent with multiple radiative environments or donor–acceptor interactions typical of RE^{3+}-doped inorganic matrices.

The decay curves were modelled using a double-exponential fitting function:

$$I(t) = A_1\, exp\left(-\frac{t}{\tau_1}\right) + A_2\, exp\left(-\frac{t}{\tau_2}\right) \quad (3)$$

where τ_1 and τ_2 denote the fast and slow decay components, respectively, and A_1, A_2 represent their relative amplitudes. The average lifetime (τ_{avg}) was determined via:

$$\tau_{avg} = \frac{A_1\tau_1^2 + A_2\tau_2^2}{A_1\tau_1 + A_2\tau_2} \quad (4)$$

As summarized in Table 3, increasing the Tb^{3+} concentration from 0.01 to 0.05 led to a notable rise in τ_{avg}.

Remarkably, co-doping with alkali ions significantly altered the decay kinetics. The addition of 0.02 Li^+ resulted in an average lifetime of 1361.61μs, which is comparable to the calculated radiative lifetime (1364.4 μs) and indicates strong suppression of nonradiative decay channels. These enhancements can be interpreted in terms of local field modification and energy level stabilization introduced by monovalent cationic perturbation, which can suppress nonradiative multiphonon processes.

To quantify the radiative efficiency of the phosphors, experimental lifetimes (τ_{avg}) were compared with theoretical radiative lifetimes (τ_{rad}) estimated from Judd–Ofelt parameters (see Section 3.9). The internal radiative efficiency (η_{rad}) was calculated using:

$$\eta_{rad} = \frac{\tau_{avg}}{\tau_{rad}} \quad (5)$$

Accordingly, the internal radiative efficiencies were determined to be 63.8% for the pristine sample, 99.8% for the Li^+-co-doped sample, and 93.8% for the Na^+-co-doped sample. These values satisfy the physically required condition $\tau_{avg} \leq \tau_{rad}$ and confirm that alkali co-doping effectively modulates the balance between radiative and nonradiative processes.

These findings establish alkali ion co-doping as an effective route to optimize lifetime characteristics and improve energy conversion efficiency in borate-based Tb^{3+} phosphors, making them suitable

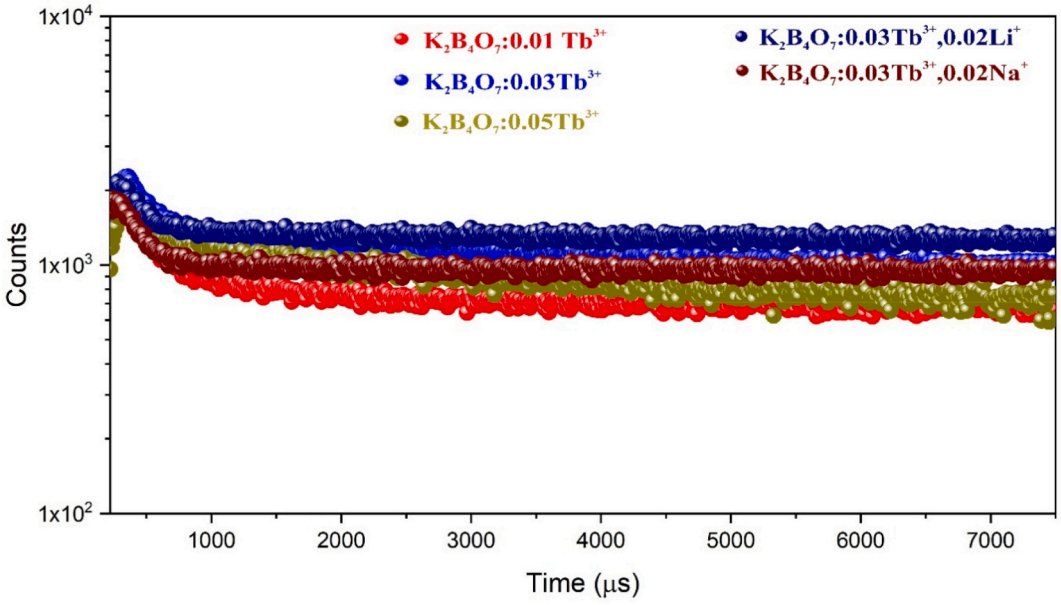

Fig. 10. Time-resolved photoluminescence decay curves of the $^5D_4 \rightarrow {}^7F_5$ transition in $K_2B_4O_7$:Tb^{3+} phosphors with and without alkali ion co-doping under 376 nm excitation.

Table 3
Biexponential decay fitting parameters and average lifetimes (τ_{avg}) for the $^5D_4 \rightarrow {}^7F_5$ transition in $K_2B_4O_7$:Tb^{3+} phosphors with varying Tb^{3+} concentrations and alkali ion co-doping under 376 nm excitation.

		Time(μs)	Rel.%	τ_{avg}(μs)	χ^2
$K_2B_4O_7$:0.01 Tb^{3+}	τ_1	14.22	10.15	1031.56	1.0258
	τ_2	2360.88	89.85		
$K_2B_4O_7$:0.03 Tb^{3+}	τ_1	14.18	41.52	2334.66	0.9137
	τ_2	1103.78	58.48		
$K_2B_4O_7$:0.05 Tb^{3+}	τ_1	14.02	33.41	2598.96	1.2801
	τ_2	2612.22	66.59		
$K_2B_4O_7$:0.03 Tb^{3+},0.02Li^+	τ_1	14.78	22.88	1361.61	0.9933
	τ_2	3460.89	77.17		
$K_2B_4O_7$:0.03 Tb^{3+},0.02Na^+	τ_1	15.96	37.44	1764.27	1.0656
	τ_2	1574.40	62.56		

candidates for long-persistence lighting and afterglow applications.

3.10. Judd–Ofelt analysis and radiative properties of Tb^{3+} transitions

The preceding structural, steady-state, and time-resolved photoluminescence analyses collectively suggest that alkali incorporation modifies both the local symmetry and relaxation dynamics of Tb^{3+} ions. To quantitatively evaluate how these structural perturbations affect radiative transition probabilities, Judd–Ofelt analysis was performed. To gain deeper insight into the radiative behavior and local crystal field environment surrounding Tb^{3+} ions in the $K_2B_4O_7$ host, Judd–Ofelt (J–O) theory was applied to the measured emission spectra. The integrated peak areas corresponding to the $^5D_4 \rightarrow {}^7F_J$ ($J = 6$–1) transitions were extracted and used to calculate oscillator strengths, radiative transition probabilities (A_J), and branching ratios (β_J), enabling quantification of electric dipole transition probabilities under varying alkali co-doping conditions.

3.11. Theoretical framework

Although the Judd–Ofelt (J–O) theory was originally developed based on absorption spectra [34,35], emission-based approaches have been widely adopted for rare-earth-doped phosphors when absorption bands are weak, overlapping, or insufficient for reliable fitting. In such cases, the radiative parameters can be extracted using fluorescence intensity analysis, as demonstrated in previous studies [7,36].

In the present work, the absorption spectrum of Tb^{3+}-doped $K_2B_4O_7$ exhibited limited and low-intensity f–f transitions, rendering conventional absorption-based fitting unreliable. Therefore, the Judd–Ofelt parameters were determined using the emission-based formalism.

The spontaneous electric-dipole transition probability for the $^5D_4 \rightarrow {}^7F_J$ transition is expressed as:

$$A_{ED}(J) = \frac{64\pi^4 e^2}{3h\lambda^3(2J+1)} \cdot \frac{n(n^2+2)^2}{9} \sum_{\lambda=2,4,6} \Omega_\lambda \langle U^\lambda \rangle^2 \quad (6)$$

where Ω_λ ($\lambda = 2, 4, 6$) are the Judd–Ofelt intensity parameters, $\langle U^\lambda \rangle^2$ are the squared reduced matrix elements, n is the refractive index of the host, and λ represents the transition wavelength.

The magnetic-dipole transition probability is given by:

$$A_{MD}(J) = \frac{64\pi^4 \nu^3}{3h(2J+1)} n^3 S_{MD} \quad (7)$$

where ν is the transition frequency and S_{MD} is the magnetic-dipole line strength.

The total radiative transition probability is obtained as:

$$A_T(J) = A_{ED}(J) + A_{MD}(J) \quad (8)$$

The radiative lifetime of the emitting level ($^5D_4$) is then calculated from the sum of all transition probabilities:

$$\tau_{rad} = \frac{1}{\sum_J A_T(J)} \quad (9)$$

The branching ratio for a given transition is defined as:

$$\beta_J = \frac{A_T(J)}{\sum_J A_T(J)} \quad (10)$$

The internal radiative efficiency was evaluated using:

$$\eta_{rad} = \frac{\tau_{exp}}{\tau_{rad}} \quad (11)$$

Using the integrated emission intensities of the $^5D_4 \rightarrow {}^7F_J$ transitions, the Judd–Ofelt intensity parameters (Ω_2 and Ω_4) were extracted

through intensity ratio analysis following the fluorescence-based formalism.

The J–O formalism models the electric dipole intensity of 4f–4f transitions using three phenomenological parameters Ω_λ ($\lambda = 2, 4, 6$), which reflect the host symmetry, ligand polarizability, and crystal field perturbation. The spontaneous emission probability for an electric dipole transition is given by:

$$A_J = \frac{64\pi^4 e^2}{3hc\lambda^3(2J'+1)} n\left(n^2+2\right)^2 \cdot S_{ed} \quad (12)$$

where λ is the emission wavelength (in cm), n is the refractive index of the host medium (assumed as 1.55), and S_{ed} is the electric dipole line strength. For each $^5D_4 \rightarrow {}^7F_J$ transition, S_{ed} is computed from:

$$S_{ed} = \sum_{\lambda=2,4,6} \Omega_\lambda \cdot \left|\left\langle {}^5D_4 \middle|\middle| U^{(\lambda)} \middle|\middle| {}^7F_J \right\rangle\right|^2 \quad (13)$$

The branching ratio and radiative lifetime are expressed as:

$$\beta_J = \frac{A_J}{\sum_J A_J}, \tau_{rad} = \frac{1}{\sum_J A_J} \quad (14)$$

The oscillator strength f_{cal} for each transition is calculated using:

$$f_{cal} = \frac{mc}{8\pi^2 e^2 N_A} \cdot \lambda^2 \cdot A_J \quad (15)$$

3.11.1. Radiative transition parameters

The radiative properties of the $^5D_4 \rightarrow {}^7F_J$ transitions in $K_2B_4O_7$:0.03 Tb^{3+} phosphors, including pristine and alkali co-doped variants (Li^+ and Na^+), were quantitatively analyzed using Judd–Ofelt formalism. The spontaneous emission probabilities (A_J), branching ratios (β_J), and calculated oscillator strengths (f_{cal}) were derived from the experimental emission spectra and the known reduced matrix elements for Tb^{3+} transitions [37]. The calculated radiative parameters are summarized in Table 3. Across all compositions, the $^5D_4 \rightarrow {}^7F_5$ transition at 541 nm exhibited the highest A_J and β_J values, indicating its dominant contribution to the total radiative decay rate. The intensity of other transitions, particularly $^5D_4 \rightarrow {}^7F_4$ and $^5D_4 \rightarrow {}^7F_6$, also showed notable sensitivity to alkali co-doping, reflecting modifications in the local symmetry and crystal field strength around the Tb^{3+} ions. The increase in A_J values observed in Li^+ and Na^+ co-doped samples compared to the pristine sample suggests that alkali ions can effectively enhance electric dipole transition probabilities by breaking inversion symmetry.

Table 4 provides a summary of the total radiative rates (ΣA_J), corresponding radiative lifetimes (τ_{rad}), experimentally measured lifetimes (τ_{exp}), and estimated internal quantum efficiencies (η_{rad}). The highest η_{rad} (≈99.8%) was achieved in the Li^+-co-doped sample, followed by the Na^+-co-doped (≈93.8%) and pristine (≈63.8%) counterparts. The internal radiative efficiency was evaluated according to $\eta_{rad} = \tau_{exp}/\tau_{rad}$. This trend indicates that alkali co-doping enhances radiative transition probabilities and suppresses nonradiative losses, with Li^+ exhibiting the highest internal radiative efficiency. In the Judd–Ofelt analysis, the refractive index (n) plays a critical role in calculating the spontaneous emission probabilities (A_J). For all radiative transition parameter estimations, a refractive index of $n = 1.55$ was adopted. This value is consistent with typical refractive indices reported for borate-based glass systems, including lithium borate glasses, which commonly exhibit values ranging between 1.50 and 1.56 depending on composition and preparation method [38].

3.11.2. Judd–Ofelt intensity parameters

Based on the theoretical framework outlined in Section 3.9.1, the Judd–Ofelt intensity parameters Ω_2 and Ω_4 were determined by non-linear least squares fitting of the experimental radiative transition probabilities (A_J) associated with the electric dipole-allowed $^5D_4 \rightarrow {}^7F_J$ transitions of Tb^{3+}. In this analysis, the magnetic dipole transition $^5D_4 \rightarrow {}^7F_5$ was employed as a reference to scale the experimental oscillator strengths. The reduced matrix elements $\langle {}^5D_4 \| U^{(\lambda)} \| {}^7F_J \rangle$ used in the calculations were taken from Carnall et al. [37].

The fitted Ω_2 and Ω_4 parameters are summarized in Table 5 for the pristine $K_2B_4O_7$:Tb^{3+} sample and for the Li^+ - and Na^+-co-doped variants. A clear enhancement in the Ω_2 parameter was observed with alkali co-doping, indicating increased asymmetry and covalency in the local environment of the Tb^{3+} ions. This effect was most pronounced for the Na^+ -co-doped sample, consistent with the stronger electric dipole transition intensities. These findings align with previous reports that alkali co-dopants—especially smaller cations—can induce local lattice distortions and break inversion symmetry, thereby increasing electric dipole transition probabilities and overall emission efficiency.

The Judd–Ofelt intensity parameters (Ω_2, Ω_4) were extracted by fitting the experimentally derived spontaneous emission probabilities (A_J) to the theoretical Judd–Ofelt model using non-linear least squares optimization. The fitted values for pristine and alkali-co-doped $K_2B_4O_7$:Tb^{3+} phosphors are presented in Table 6. The Ω_6 parameter was neglected in the present analysis due to its minimal contribution to the $^5D_4 \rightarrow {}^7F_J$ transitions of Tb^{3+} and the limited sensitivity of the experimental dataset to higher-rank tensor components, as commonly reported for Tb^{3+}-activated the other hosts [39].

The gradual enhancement of the Ω_2 parameter with increasing alkali content reflects an increase in the asymmetry and covalency of the local environment around the Tb^{3+} ions. This effect is most pronounced for the Na^+ -co-doped sample, consistent with the observed intensification

Table 5
Summary of the total spontaneous emission probabilities (ΣA_J), radiative lifetimes (τ_{rad}), experimentally measured decay times (τ_{exp}), and calculated internal quantum efficiencies (η_{rad}) for $K_2B_4O_7$:0.03 Tb^{3+} phosphors, including pristine and alkali (Li^+, Na^+) co-doped compositions.

Sample	$\sum A_J$ (s^{-1})	τ_{rad} (μs)	τ_{exp} (μs)	η_{rad}
$K_2B_4O_7$:0.03 Tb^{3+}	272.5	3670.8	2334.66	0.638
$K_2B_4O_7$:0.03 Tb^{3+}, 0.02Li^+	732.8	1364.4	1361.61	0.998
$K_2B_4O_7$:0.03 Tb^{3+}, 0.02Na^+	533.7	1873.1	1764.27	0.938

Table 4
Radiative parameters including spontaneous emission probabilities (A_J), branching ratios (β_J), and calculated oscillator strengths (f_{cal}) for the $^5D_4 \rightarrow {}^7F_J$ transitions of Tb^{3+} in $K_2B_4O_7$ host matrices: pristine and co-doped with Li^+ and Na^+ ions. Calculations are based on experimental peak areas and standard reduced matrix elements for Tb^{3+} transitions.

Transition	λ(nm)	$A_J(s^{-1})$ Tb^{3+} doped	$A_J(s^{-1})$ +Li^+	$A_J(s^{-1})$ +Na^+	β_J Tb^{3+} doped	β_J +Li^+	β_J +Na^+	f_{cal} (× 10^{-6}) Tb^{3+} doped	f_{cal} (× 10^{-6}) +Li^+	f_{cal} (× 10^{-6}) +Na^+
$^5D_4 \rightarrow {}^7F_6$	487	21.6	85.2	99.2	0.079	0.116	0.185	1.71	2.52	4.31
$^5D_4 \rightarrow {}^7F_5$	541	64.2	218.6	262.7	0.236	0.298	0.490	5.11	6.45	10.6
$^5D_4 \rightarrow {}^7F_4$	585	29.3	91.8	124.1	0.108	0.125	0.232	2.34	2.71	5.74
$^5D_4 \rightarrow {}^7F_3$	622	29.3	92.7	27.9	0.108	0.127	0.052	2.34	2.75	1.31
$^5D_4 \rightarrow {}^7F_2$	652	5.9	20.1	12.6	0.022	0.027	0.023	0.48	0.58	0.49
$^5D_4 \rightarrow {}^7F_1$	671	23.2	28.6	7.2	0.085	0.039	0.014	1.84	0.85	0.29
Total	—	272.5	732.8	533.7	—					—

Table 6
Judd–Ofelt intensity parameters (Ω_λ, $\lambda = 2, 4$) for $K_2B_4O_7$:0.03 Tb^{3+} with and without alkali ion co-doping.

Sample	Ω_2 ($\times 10^{-20}$ cm^2)	Ω_4 ($\times 10^{-20}$ cm^2)
$K_2B_4O_7$:0.03 Tb^{3+}	2.41	1.73
+0.02Li+	3.87	2.04
+0.02Na+	4.52	2.27

of electric dipole transitions. These results support prior findings that alkali ions—particularly those with smaller ionic radii—can induce local structural distortions and break inversion symmetry, thereby enhancing electric dipole transition probabilities [31].

Following the extraction of the Judd–Ofelt intensity parameters (Ω_2 and Ω_4), a more detailed transition-level analysis was carried out to explicitly present the input and output quantities involved in the emission-based radiative calculations. To improve clarity and ensure full transparency of the methodology, the squared reduced matrix elements together with the integrated emission band areas are summarized in Table 7. The corresponding electric-dipole (A_{ED}), magnetic-dipole (A_{MD}), and total radiative transition probabilities (A_T) for each $^5D_4 \rightarrow {}^7F_J$ transition are presented separately in Table 8.

The transition-resolved radiative analysis (Tables 7 and 8) confirms that alkali co-doping systematically modifies both electric- and magnetic-dipole transition probabilities within the $^5D_4$ manifold. In particular, the enhancement of selected radiative channels, together with the suppression of non-radiative decay pathways observed in the lifetime measurements, clearly indicates cooperative modulation of the local crystal-field environment and phonon-assisted relaxation processes.

When these radiative findings are considered alongside the structural refinement results, concentration-dependent emission behavior, and thermal quenching analysis, a coherent and internally consistent structure–property correlation emerges. The combined structural perturbation induced by Tb^{3+} substitution and alkali co-doping leads to crystal-field modulation and phonon coupling regulation, which collectively govern radiative branching probabilities, non-radiative relaxation, and thermometric response behavior. Based on these collective findings, a unified microscopic mechanism describing the role of alkali co-doping in $K_2B_4O_7$:Tb^{3+} phosphors is proposed (Fig. 11).

This schematic illustrates how Tb^{3+} substitution and alkali co-doping cooperatively induce local crystal-field modulation and phonon coupling regulation. These structural perturbations suppress defect-assisted non-radiative pathways, modify radiative branching probabilities within the $^5D_4$ manifold, and tune the thermal quenching activation energy. The interplay of these effects explains both the concentration-dependent emission evolution and the anti-correlated green–red thermal response observed experimentally.

3.11.3. Radiative efficiency and spectroscopic implications

Combining τ_{rad} from Judd–Ofelt theory with τ_{avg} obtained from decay measurements (Section 3.XI), internal radiative efficiency (η_{rad}) values were determined using $\eta_{rad} = \tau_{avg}/\tau_{rad}$. The Li^+-co-doped sample exhibited were determined using $\eta_{rad} = \tau_{avg}/\tau_{rad}$. The Li^+-co-doped sample exhibited the highest efficiency ($\eta_{rad} \approx 99.8\%$), followed by the Na^+-co-doped (≈93.8%) and pristine (≈63.8%) compositions.

Table 8
Electric dipole (A_{ED}), magnetic dipole (A_{MD}), and total radiative transition probabilities (A_T).

Transition	Sample	A_{ED} (s^{-1})	A_{MD} (s^{-1})	A_T (s^{-1})
$^5D_4 \rightarrow {}^7F_6$	0.03 Tb^{3+}	21.6	0	21.6
	$+Li^+$	85.2	0	85.2
	$+Na^+$	99.2	0	99.2
$^5D_4 \rightarrow {}^7F_5$	0.03 Tb^{3+}	0	64.2	64.2
	$+Li^+$	0	218.6	218.6
	$+Na^+$	0	262.7	262.7
$^5D_4 \rightarrow {}^7F_4$	0.03 Tb^{3+}	29.3	0	29.3
	$+Li^+$	91.8	0	91.8
	$+Na^+$	124.1	0	124.1
$^5D_4 \rightarrow {}^7F_3$	0.03 Tb^{3+}	29.3	0	29.3
	$+Li^+$	92.7	0	92.7
	$+Na^+$	27.9	0	27.9
$^5D_4 \rightarrow {}^7F_2$	0.03 Tb^{3+}	5.9	0	5.9
	$+Li^+$	20.1	0	20.1
	$+Na^+$	12.6	0	12.6
$^5D_4 \rightarrow {}^7F_1$	0.03 Tb^{3+}	23.2	0	23.2
	$+Li^+$	28.6	0	28.6
	$+Na^+$	7.2	0	7.2

The substantial enhancement in η_{rad} upon alkali incorporation indicates effective suppression of non-radiative relaxation pathways and improved radiative branching within the $^5D_4$ manifold, particularly for the dominant $^5D_4 \rightarrow {}^7F_5$ transition. This improvement in radiative efficiency is consistent with the observed increase in green emission intensity and the modified thermal quenching behavior. These results confirm that alkali-induced lattice perturbation not only tunes crystal-field symmetry but also optimizes spectroscopic performance, providing a viable route for enhancing emission efficiency in borate-based Tb^{3+} phosphors.

3.12. Colorimetric properties and CIE chromaticity analysis

The chromaticity coordinates of $K_2B_4O_7$:Tb^{3+} phosphors were evaluated using the CIE 1931 color space to assess the color stability and tunability as a function of Tb^{3+} concentration and alkali co-doping. Fig. 12a shows the CIE coordinates of $K_2B_4O_7$:xTb^{3+} samples, where all compositions are located in the green region, consistent with the dominance of the Tb^{3+} $^5D_4 \rightarrow {}^7F_5$ transition. A slight shift of the chromaticity points with increasing Tb^{3+} content is observed, reflecting minor variations in the relative contribution of secondary Tb^{3+} emission lines, while preserving the overall green emission character.

Fig. 12b and c presents the CIE chromaticity diagrams of $K_2B_4O_7$:0.03 Tb^{3+} phosphors co-doped with Li^+ and Na^+, respectively. In both cases, the chromaticity coordinates remain clustered within a narrow region of the green domain. This confirms that alkali co-doping maintains the dominant $^5D_4 \rightarrow {}^7F_5$ transition while causing only subtle chromaticity shifts. The correlated color temperature (CCT), estimated using McCamy's empirical method [40], increases from approximately 5380 K for the undoped sample to 5557 K and 5749 K for Li^+- and Na^+-co-doped samples, respectively, indicating a slight blue shift consistent with the displacement of the chromaticity coordinates toward lower *x* values. The absence of noticeable color drift confirms that Li^+ and Na^+ incorporation preserves excellent chromatic stability while improving luminescence performance.

Table 7
Squared reduced matrix elements and normalized integrated emission areas ($\times 10^5$).

Transition	λ (nm)	$\langle U(2)\rangle^2$	$\langle U(4)\rangle^2$	$\langle U(6)\rangle^2$	Peak Area (Pristine)	Peak Area (Li^+)	Peak Area (Na^+)
$^5D_4 \rightarrow {}^7F_6$	487	0.0021	0.0008	0.0013	2.93	11.64	13.19
$^5D_4 \rightarrow {}^7F_5$	541	0.0153	0.0014	0.0022	8.70	29.86	33.64
$^5D_4 \rightarrow {}^7F_4$	585	0.0003	0.0022	0.0013	3.98	12.53	13.46
$^5D_4 \rightarrow {}^7F_3$	622	0.0023	0.0005	0.0006	3.99	12.66	14.54
$^5D_4 \rightarrow {}^7F_2$	652	0.0011	0.0004	0.0001	0.80	2.75	4.17
$^5D_4 \rightarrow {}^7F_1$	671	0.0000	0.0025	0.0000	3.53	6.73	8.56

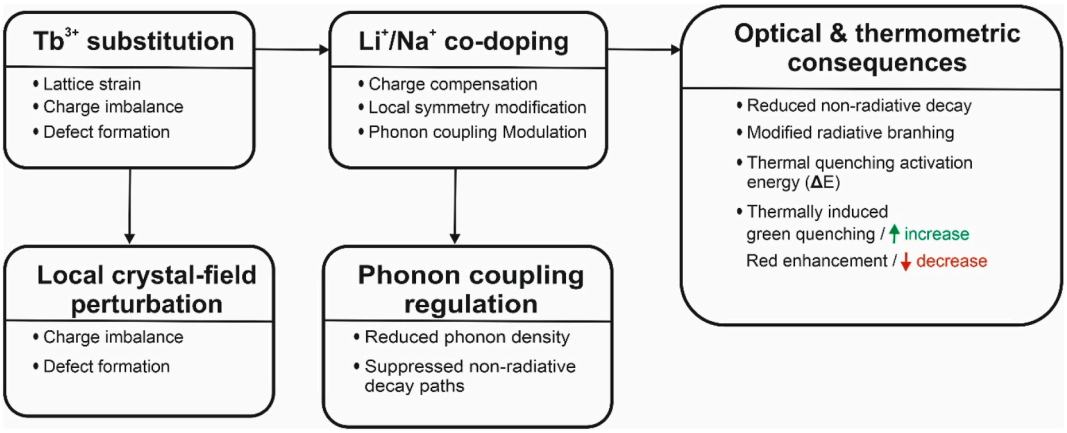

Fig. 11. Schematic illustration of the alkali-modulated structure–property correlation in $K_2B_4O_7$:Tb^{3+} phosphors. Tb^{3+} substitution induces lattice strain and defect formation, while Li^+/Na^+ co-doping regulates local symmetry and phonon coupling.

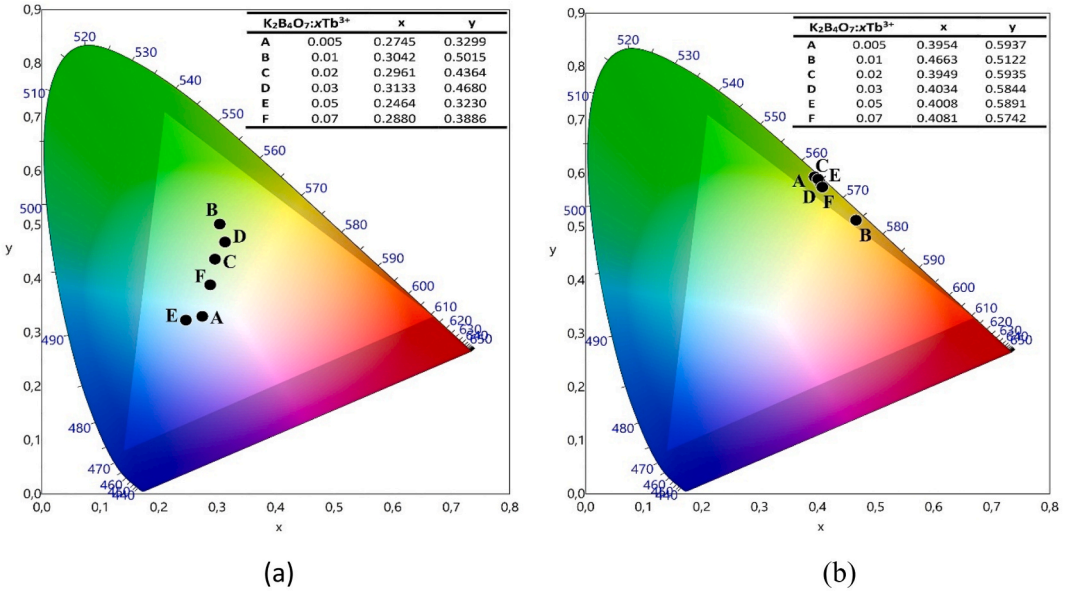

Fig. 12. CIE 1931 chromaticity coordinates of **(a)** $K_2B_4O_7$:xTb^{3+}, **(b)** $K_2B_4O_7$:0.03 Tb^{3+}, yLi^+, and **(c)** $K_2B_4O_7$:0.03 Tb^{3+}, yNa^+ phosphors under 377 nm excitation.

Notably, the optimal co-doping concentration ($y = 0.02$ for both Li^+ and Na^+) yields the highest emission intensity without inducing perceptible changes in color coordinates. This combination of intensity enhancement and chromatic stability is particularly advantageous for solid-state lighting applications, where both brightness and color consistency are critical. Overall, the CIE analysis demonstrates that $K_2B_4O_7$:Tb^{3+} phosphors exhibit robust green emission with minimal color variation across different activator and co-dopant concentrations, underscoring their suitability for high-performance green-emitting phosphors in solid-state lighting and LED-based applications.

4. Conclusions

This study demonstrates that alkali co-doping in $K_2B_4O_7$:Tb^{3+} enables controlled modulation of radiative and non-radiative relaxation dynamics through subtle lattice perturbations rather than structural phase alteration. Concentration quenching is governed by dipole–quadrupole multipolar interactions, while Judd–Ofelt analysis confirms that alkali incorporation enhances electric-dipole transition probabilities via local crystal-field symmetry modification. The system exhibits a critical transfer distance of ~15.46 Å and a thermally activated red emission enhancement of approximately 30-fold between 300 and 550 K.

Time-resolved photoluminescence and radiative rate analysis further demonstrated that alkali ions actively modulate radiative and non-radiative relaxation, allowing controlled tuning of $^5D_4$ lifetime and internal quantum efficiency. Notably, Li^+ and Na^+ co-doping exert distinct influences on the thermal quenching behavior, reflecting their different impacts on lattice rigidity and phonon coupling. Temperature-dependent photoluminescence measurements uncovered an unusual anti-correlated thermal response, wherein the dominant green emission undergoes conventional thermal quenching while a red emission band centered at ~670 nm exhibits a pronounced thermally activated enhancement. This behavior originates from temperature-induced radiative branching redistribution within the $^5D_4$ manifold, facilitated by phonon-assisted symmetry relaxation and defect-mediated energy feeding. Collectively, the combined structural, steady-state, time-resolved, and Judd–Ofelt analyses establish a unified microscopic mechanism in which alkali incorporation simultaneously modulates defect density, electron–phonon coupling strength, multipolar interaction efficiency, and intra-manifold radiative branching probabilities.

This mechanistic insight provides a rational framework for lattice-perturbation-driven emission engineering in borate phosphors and demonstrates the feasibility of single-ion, non-thermally coupled Tb^{3+} systems as intrinsically stable platforms for ratiometric optical thermometry.

CRediT authorship contribution statement

Abeer S. Altowyan: Writing – original draft, Methodology, Investigation, Formal analysis. **M.B. Coban:** Methodology, Investigation, Funding acquisition. **U.H. Kaynar:** Methodology, Investigation, Funding acquisition, Formal analysis. **S. Cam Kaynar:** Methodology, Investigation. **T. Karaman:** Methodology, Investigation, Formal analysis. **Jabir Hakami:** Methodology, Investigation, Conceptualization. **H. Aydin:** Software, Methodology, Investigation. **N. Can:** Writing – review & editing, Writing – original draft, Supervision.

Declaration of competing interest

The authors declare that they have no known competing financial interests or personal relationships that could have appeared to influence the work reported in this paper.

Acknowledgements

This work was also supported by Izmir Bakırçay University Scientific Research Projects Coordination Unit, under grant number HZP.2025.004. This study was supported by the Princess Nourah bint Abdulrahman University Researchers Supporting Project number (PNURSP2026R16), Princess Nourah bint Abdulrahman University, Riyadh, Saudi Arabia. This study was also financially supported by the Scientific and Technological Research Council of Turkey (TÜBITAK, Project No. 223M036).

References

[1] R. Sonekar, Inorganic Borate Host Luminescent Materials: Preparation, Photoluminescence Studies and Applications, Lambert Academic Publishing, 2011.
[2] A. Tiwari, S.J. Dhoble, Borate-based luminescent materials: a comprehensive review of structural influences on thermal stability and luminescence characteristics, J. Lumin. 287 (2025) 121490, https://doi.org/10.1016/j.jlumin.2025.121490.
[3] V.R. Panse, S.P. Hargunani, A. Saregar, S.M. Waghare, A. Hadap, S.V. Dewalkar, Y. Yuberti, Analyzing the photoluminescence and energy transfer in $Sr_3Gd(BO_3)_3$: inorganic borate-based phosphor Eu^{3+}, Tb^{3+} and Ce^{3+}, J. Opt. (2024) https://doi.org/10.1007/s12596-024-02077-5.
[4] J. Hakami, Ü.H. Kaynar, M. Ayvacikli, M.B. Coban, J. Garcia-Guinea, P. D. Townsend, M. Oglakci, N. Can, Structural and temperature-dependent luminescence of terbium doped $YAl_3(BO_3)_4$ phosphor synthesized by the combustion method, Ceram. Int. 48 (2022) 32256–32265, https://doi.org/10.1016/j.ceramint.2022.07.167.
[5] O. Ayari, C. Bouzidi, F. Khlissa, A. Garbout, S. Hraiech, Investigation of spectroscopic properties of Sm^{3+} doped phosphate glasses for reddish orange light applications, Displays 74 (2022) 102266, https://doi.org/10.1016/j.displa.2022.102266.
[6] A. Abdallah, C. Bouzidi, Optical studies of Dy_2O_3 doped phosphate glasses for potential white luminescence applications, Solid State Sci. 165 (2025) 107958, https://doi.org/10.1016/j.solidstatesciences.2025.107958.
[7] C. Bouzidi, M. Ferhi, H. Elhouichet, M. Ferid, Spectroscopic properties of rare-earth (Eu^{3+}, Sm^{3+}) doped $BaWO_4$ powders, J. Lumin. 161 (2015) 448–455, https://doi.org/10.1016/j.jlumin.2015.01.053.
[8] M. Ben Mohamed, N. Hsouna, C. Bouzidi, C. Hernández-Álvarez, I.R. Martín, Temperature sensing and energy transfer processes in Pr^{3+}-Yb^{3+} co-doped phosphate glasses, Opt. Mater. 162 (2025) 116811, https://doi.org/10.1016/j.optmat.2025.116811.
[9] G. Blasse, B.C. Grabmaier, Luminescent Materials, Springer, 1994.
[10] Z. Xiong, Q. Tang, C. Zhang, Investigation of thermoluminescence in $Li_2B_4O_7$ phosphors doped with Cu, Ag and Mg, Sci. China G 50 (2007) 311–320, https://doi.org/10.1007/s11433-007-0020-3.
[11] S. Jipa, W. Kappel, T. Zaharescu, L.M. Gorghiu, C. Dumitrescu, Activation energy from thermoluminescence of $K_2B_4O_7$ doped with Cu and Ag, Rev. Chim. 59 (2008) 300–303, https://doi.org/10.37358/RC.08.3.1752.
[12] R. Hemam, L.R. Singh, S.D. Singh, R.N. Sharan, Preparation of CaB_4O_7 nanoparticles doped with different concentrations of Tb^{3+}:Photoluminescence and thermoluminescence/optically stimulated luminescence study, J. Lumin. 197 (2018) 399–405, https://doi.org/10.1016/j.jlumin.2018.01.062.
[13] R. Mohan P, S.K. Jose, A. George, N.V. Unnikrishnan, C. Joseph, P.R. Biju, Synthesis and photoluminescence characteristics of near white light emitting CaB_2O_4:Dy^{3+}, Li^+ phosphor, J. Phys. Chem. Solid. 119 (2018) 166–174, https://doi.org/10.1016/j.jpcs.2018.03.039.
[14] A.S. Altowyan, U.H. Kaynar, H. Aydin, J. Hakami, M.B. Coban, K. Cikrikci, M. Ayvacikli, N. Can, Synthesis, structural characterization, and photoluminescence properties of Dy^{3+}-Doped CaB_4O_7 phosphors: influence of Li^+ and K^+ Co-doping, Mater. Sci. Semicond. Process. 195 (2025) 109593, https://doi.org/10.1016/j.mssp.2025.109593.
[15] A. Tuomela, M. Zhang, M. Huttula, S. Sakirzanovas, A. Kareiva, A.I. Popov, A. P. Kozlova, S.A. Aravindh, W. Cao, V. Pankratov, Luminescence and vacuum ultraviolet excitation spectroscopy of samarium doped SrB4O7, J. Alloys Compd. 826 (2020) 154205, https://doi.org/10.1016/j.jallcom.2020.154205.
[16] J.L.O. Santos, A.S. Souza, J.V.B. Valença, H. Trombini, C. Radtke, I.S. Silveira, R. G. Fernandes, H. Lima, New insights into the role of the doping process on the luminescence properties of MgB_4O_7:Ce,Li, J. Alloys Compd. 1036 (2025) 181217, https://doi.org/10.1016/j.jallcom.2025.181217.
[17] M.B. Coban, A.S. Altowyan, U.H. Kaynar, J. Hakami, H. Aydin, I. Kara, A. Canimoglu, N. Can, Enhanced photoluminescence, thermal stability, and anti-thermal quenching in Li^+/Na^+ Co-doped $K_2B_4O_7$:Dy^{3+} phosphors for solid state lighting, Ceram. Int. (2026), https://doi.org/10.1016/j.ceramint.2026.01.181.
[18] Y.A. Rasdi, M.H.M. Zaid, K.A. Matori, Y.W. Fen, Z.W. Loh, Thulium-doped magnesium borotellurite glasses: fabrication, optical properties and photoluminescence performance, Results Eng. 28 (2025) 107452, https://doi.org/10.1016/j.rineng.2025.107452.
[19] L. Jun, X. Shuping, G. Shiyang, FT-IR and Raman spectroscopic study of hydrated borates, Spectrochim. Acta Part A Mol. Biomol. Spectrosc. 51 (1995) 519–532, https://doi.org/10.1016/0584-8539(94)00183-C.

[20] G. Padmaja, P. Kistaiah, Infrared and raman spectroscopic studies on alkali borate glasses: evidence of mixed alkali effect, J. Phys. Chem. A 113 (2009) 2397–2404, https://doi.org/10.1021/jp809318e.
[21] M.A. Morsy, T.F. Garrison, M.R. Kessler, M.H.A. Mhareb, H.Z. El-Deen, Structural elucidation of lithium borate glasses using XRD, FTIR, and EPR spectroscopy, ACS Phys. Chem. Au 5 (2025) 227–238, https://doi.org/10.1021/acsphyschemau.4c00106.
[22] G. Souadi, U.H. Kaynar, M. Ayvacikli, M.B. Coban, M. Oglakci, A. Canimoglu, N. Can, Synthesis and photoluminescence characteristics of a novel Eu and Tb doped Li_2MoO_4 phosphor, Appl. Radiat. Isot. 175 (2021) 109820, https://doi.org/10.1016/j.apradiso.2021.109820.
[23] H. Liu, H. Wang, C. Sun, H. Tian, Q. Wang, H. Zhu, X. Yang, Y. Zhang, K+ Co-doped Ca_2LaTaO_6: RE^{3+}(RE=Pr, Tb) phosphors: enhancement photoluminescence intensity and high thermal stability, Ceram. Int. 51 (2025) 32701–32710, https://doi.org/10.1016/j.ceramint.2025.05.004.
[24] R. Kiran, S.M.M. Kennedy, A. Princy, M.I. Sayyed, A.H. Almuqrin, S.D. Kamath, Negative thermal quenching and optically stable Tb^{3+}-doped tungstate phosphor for high temperature lighting and advanced thermometry applications, Mater. Adv. 6 (2025) 9746–9760, https://doi.org/10.1039/D5MA00655D.
[25] A. Fujii, K. Miyazaki, Y. Takebuchi, T. Kato, D. Nakauchi, N. Kawaguchi, T. Yanagida, Photoluminescence and thermoluminescence properties of undoped and Tb-doped $Ca_2Al_2SiO_7$ single crystals for dosimetric applications, Radiat. Phys. Chem. 242 (2026) 113620, https://doi.org/10.1016/j.radphyschem.2026.113620.
[26] R. Kokate, G.B. Nair, S.J. Dhoble, H. Jeong, H. Jeong, R. Boddula, V. Singh, UV and VUV induced luminescence in Tb^{3+} doped $Ca_3La_3(BO_3)_5$ phosphors for PDP applications, Optik 241 (2021) 166633, https://doi.org/10.1016/j.ijleo.2021.166633.
[27] I.-E. Kwon, B.-Y. Yu, H. Bae, Y.-J. Hwang, T.-W. Kwon, C.-H. Kim, C.-H. Pyun, S.-J. Kim, Luminescence properties of borate phosphors in the UV/VUV region, J. Lumin. 87–89 (2000) 1039–1041, https://doi.org/10.1016/S0022-2313(99)00532-3.
[28] R.P. Rao, Tb^{3+} activated green phosphors for plasma display panel applications, J. Electrochem. Soc. 150 (2003) H165, https://doi.org/10.1149/1.1583718.
[29] N. Dhananjaya, H. Nagabhushana, B.M. Nagabhushana, B. Rudraswamy, C. Shivakumara, K. Narahari, R.P.S. Chakradhar, Enhanced photoluminescence of Gd_2O_3:Eu^{3+} nanophosphors with alkali (M=Li^+, Na^+, K^+) metal ion co-doping, Spectrochim. Acta Part A Mol. Biomol. Spectrosc. 86 (2012) 8–14, https://doi.org/10.1016/j.saa.2011.05.072.
[30] A.A. Alsam, U.H. Kaynar, H. Aydin, M.B. Coban, A. Canimoglu, N. Can, Enhanced luminescence and quenching mechanisms in Na^+ Co-doped $K_7CaY_2(B_5O_{10})_3$:Tb^{3+} phosphors under UV radiation, Appl. Radiat. Isot. 217 (2025) 111635, https://doi.org/10.1016/j.apradiso.2024.111635.
[31] M.B. Coban, U.H. Kaynar, A.S. Altowyan, J. Hakami, H. Aydin, A. Canimoglu, N. Can, Judd–Ofelt analysis and negative thermal quenching behavior of Tb^{3+}-activated $Ca_3La_3(BO_3)_5$ phosphors co-doped with alkali ions for high-temperature photonic applications, Sensors Actuators A Phys 395 (2025) 117109, https://doi.org/10.1016/j.sna.2025.117109.
[32] C. Wang, Y. Jin, R. Zhang, Q. Yao, Y. Hu, A review and outlook of ratiometric optical thermometer based on thermally coupled levels and non-thermally coupled levels, J. Alloys Compd. 894 (2022) 162494, https://doi.org/10.1016/j.jallcom.2021.162494.
[33] S. Lig, H. Muji, Y. Zhang, X. Zhou, K. Wang, Z. Wang, Q. Tian, K. Chao, Design and synthesis of $Sr_3TaGa_3Si_2O_{14}$:Tb^{3+},Eu^{3+} phosphors for enhanced optical thermometry and multicolor anti-counterfeiting applications, Ceram. Int. 50 (2024) 53264–53271, https://doi.org/10.1016/j.ceramint.2024.10.176.
[34] B.R. Judd, Optical absorption intensities of rare-earth ions, Phys. Rev. 127 (1962) 750–761, https://doi.org/10.1103/PhysRev.127.750.
[35] G.S. Ofelt, Intensities of crystal spectra of rare-earth ions, J. Chem. Phys. 37 (1962) 511–520, https://doi.org/10.1063/1.1701366.
[36] S.C. Kaynar, A.S. Altowyan, H. Aydin, U.H. Kaynar, M.B. Coban, J. Hakami, N. Can, Judd–Ofelt analysis and photoluminescence behavior of Tb^{3+}-activated $K_7SrY_2(B_5O_{10})_3$ phosphors modified with alkali co-dopants for solid-state lighting applications, Spectrochim. Acta Part A Mol. Biomol. Spectrosc. 341 (2025) 126435, https://doi.org/10.1016/j.saa.2025.126435.
[37] W.T. Carnall, G.L. Goodman, K. Rajnak, R.S. Rana, A systematic analysis of the spectra of the lanthanides doped into single crystal LaF_3, J. Chem. Phys. 90 (1989) 3443–3457, https://doi.org/10.1063/1.455853.
[38] V.T. Adamiv, Y.V. Burak, R.V. Gamernyk, G.M. Romanyuk, I.M. Teslyuk, Optical properties, electronic polarizability and optical basicity of lithium borate glasses, Phys. Chem. Glas. - Eur. J. Glas. Sci. Technol. Part B 52 (2011) 152–156.
[39] L. Wang, Y. Zhang, D. Gao, X. Sha, X. Chen, Y. Zhang, J. Zhang, X. Zhang, Y. Cao, Y. Wang, X. Li, S. Xu, H. Yu, B. Chen, Luminescence properties and Judd–Ofelt analysis of Tb^{3+} doped Sr_2YTaO_6 double perovskite phosphors for white LED applications, Dalton Trans. 53 (2024) 6399–6409, https://doi.org/10.1039/D4DT00302K.
[40] C.S. McCamy, Correlated color temperature as an explicit function of chromaticity coordinates, Color Res. Appl. 17 (1992) 142–144, https://doi.org/10.1002/col.5080170211.